SAPIENZA
UNIVERSITÀ DI ROMA

The electron spectrometer of the PlasmonX experiment: from the design to the operation

Scuola di dottorato in Scienze Astronomiche, Chimiche Fisiche e Matematiche "Vito Volterra"

Dottorato di Ricerca in Fisica – XXIV Ciclo

Candidate

Nadejda Vassileva Drenska
ID number 696991

Thesis Advisor

Prof. Riccardo Faccini

A thesis submitted in partial fulfillment of the requirements
for the degree of Doctor of Philosophy in Physics

October 2011

Thesis not yet defended

Nadejda Vassileva Drenska. *The electron spectrometer of the PlasmonX experiment: from the design to the operation.*
Ph.D. thesis. Sapienza – University of Rome

ISBN: 000000000-0

EMAIL: nadejda.drenska@roma1.infn.it

Contents

Introduction

The demise of the Superconducting Super Collider (SSC) in 1994 has re-motivated the search for alternatives to conventional particle accelerator technology, currently approaching its limit with the Large Hadron Collider (LHC) project at CERN. It has been realized since same time that plasma could form the basis of a new generation of compact accelerators thanks to its ability to support much larger electric fields.

Indeed the limiting aspect of the conventional radio-frequency cavities used to accelerate particles is the maximum sustainable accelerating field. The need to reduce both the dimensions and the costs of the accelerating machines opened a new field concerning the new acceleration techniques.

At the end of the 70's, Tajima and Dowson argued that *plasma wakefields* can provide an acceleration gradient as high as 100 GeV/m, i.e. thee order of magnitude greater with respect to what we have in conventional accelerators.

If the laser parameters are chosen to be resonant with the characteristic plasma oscillations, the plasma electrons can be pushed forward by the laser in the same direction as the laser propagation. This scheme is called *laser wake field acceleration*.

In the last 20 years the laser technology reached the required characteristics for the plasma acceleration, i.e. high intensity (I>10^{16}W/cm^2) and ultra short pulse duration (∼fs). The ideas proposed by Tajima and Dowson has been experimentally demonstrated mainly by the group located at the Rutherford Appleton Laboratory (RAL) in the United Kingdom, the group at the Laboratoire d'Optique Appliquee (LOA) in France and the group located at the Lawrence Berkeley National Laboratory (LBNL) in the United States.

The PlasmonX project at the Laboratori Nazionali di Frascati was proposed in 2008. Concerning the plasma acceleration, the main purpose of the project consists in R&D activity aimed at demonstrate the high-gradient acceleration technique by the use FLAME, an ultra-short, high power laser system. The first experiments performed in 2010 demonstrates that the accelerating regime has been achieved, but the beam quality needs to be improved for further applications.

The central topic of this thesis is the design, construction and commissioning of the device we use to characterize the accelerated electrons. As expected from simulation codes that investigates the interaction of a laser pulse with a preformed plasma, the accelerated electron bunch has peculiar characteristics and it is extremely challenging to realize a device capable to fit all of them. We expect energy spread over three order of magnitude (from few MeV to the GeV region), a significant angular divergence at low energy (∼10 mrad) and a huge number of particles ($\sim 10^9$) to detect at the same time. Considering these aspects we have designed, realized and operate an electron spectrometer that is largely described in this work.

The first chapter describes the general framework of the laser matter interaction, focusing the attention not only at the mathematical formulations but also providing an historical overview of the experimental results obtained all over the word.

The second chapter presents the global PlasmonX project and the experiment dedicated to laser-plasma acceleration. The general layout is described, all the operational parameters are given and what is expected to observe is discussed.

The third chapter is centered on the design of the spectrometer we realized. All the components are defined and the complete signal path is followed. The data acquisition and the data analysis programs are discussed. The chapter ends with the simulations of the expected signal on the spectrometer.

The forth chapter is the performance of the electron spectrometer as quantified in a series of tests done in laboratory and at the Beam Test Facility.

The last chapter presents the first experimental results as obtained in the data taking of 2010.

Chapter 1

Laser-matter interaction

Plasma-based accelerators [1] are of great interest because of their ability to sustain extremely large acceleration gradients. These accelerators have the potential to produce extremely short electron bunches which are intrinsically synchronized with the laser pulse itself, enabling a wide variation of pump-probe applications. This new accelerating technique can overcome many of the fundamental limitations that restrict acceleration in vacuum because of the fact that the plasma can be fully pre-ionized avoiding ionization and break-down effects [2].

In plasma based accelerators, acceleration is the result of the axial field of the plasma wave and not the laser field directly: the plasma converts the transverse laser field into the longitudinal electric field of the plasma wave [3]. Furthermore, the accelerating wavelength is the plasma wavelength λ_p, depending in the plasma density n_e. The condition for the growth of the plasma wave requires λ_p to be equal to the laser pulse length λ_L. Plasma based acceleration methods are, however, subject to their own intrinsic limitations, such as restrictions arising from electron dephasing, pump depletion and laser-plasma instabilities.

All these aspects will be quantified in this chapter.

1.1 The physics of laser-plasma acceleration

1.1.1 The plasma characteristics

The starting point to explore plasma based acceleration is the definition of plasma. As given by [4], we can state that a plasma is a quasi-neutral gas of charged and neutral particles which exhibits collective behavior.

The term quasi-neutral refers to the fundamental characteristic of the behavior of a plasma which is its ability to shield out electron potentials that are applied to it. The quantity called Debye length λ_D is a measure of the shielding distance: a typical plasma dimension L is usually much larger than λ_D, so that whenever local concentrations of charge arise these are shielded out in a distance short compared to L [5]. This allows to take $n_i \sim n_e \sim n$, where n is a common density called the plasma density.

Collective behavior means that the motion depends not only on local conditions but on the state of the plasma also in remote regions. Since the long-range electromagnetic forces dominate ever the local collisions the latter can be neglected.

One of the fundamental parameters of a plasma is the *plasma frequency*. In order to derive its expression we have to consider the motion of the electrons in a plasma when displaced from a uniform background of ions. Immediately an electric filed will arise and pull the electrons back to their original position: because of the electron inertia, an oscillation around the ions (assumed at rest because of their heavier mass) will take place. Neglecting the magnetic field, we can write the equation of motion and continuity as:

$$\begin{aligned} mn_e[\frac{\partial \vec{v}_e}{\partial t} + (\vec{v}_e \cdot \vec{\nabla})\vec{v}_e] &= -en_e\vec{E} && (1.1) \\ \frac{\partial n_e}{\partial t} + \vec{\nabla} \cdot (n_e \vec{v}_e) &= 0 && (1.2) \end{aligned}$$

where m, n_e and $\vec{v}_e$ are the electron mass, density and velocity respectively; $\vec{E}$ is the electric field. Here the local deviation from the neutrality is the key point: Poisson's equation gives

$$\epsilon_0 \vec{\nabla} \cdot \vec{E} = e(n_i - n_e) \tag{1.3}$$

The easiest way to solve the problem is to separate the electron velocity v_e, the electron density n_e as well as the electric field in an equilibrium part indicated with 0 and a perturbation part indicated by 1:

$$n_e = n_0 + n_1, \qquad \vec{v}_e = \vec{v}_0 + \vec{v}_1, \qquad \vec{E} = \vec{E}_0 + \vec{E}_1 \tag{1.4}$$

Assuming an uniform neutral plasma at rest (before the electrons are displaced) we can set:

$$\vec{\nabla} n_0 = \vec{v}_0 = \vec{E}_0 = 0 \tag{1.5}$$

$$\frac{\partial n_0}{\partial t} = \frac{\partial \vec{v}_0}{\partial t} = \frac{\partial \vec{E}_0}{\partial t} = 0 \tag{1.6}$$

The linear theory allows to rewrite eq. 1.1–1.2 as:

$$m\frac{\partial \vec{v}_1}{\partial t} = -e\vec{E}_1 \tag{1.7}$$

$$\frac{\partial n_1}{\partial t} + n_0 \vec{\nabla} \cdot \vec{v}_1 = 0 \tag{1.8}$$

In eq.1.3 we note that $n_{i0} = n_{e0}$ because of the initial equilibrium and that $n_{i1} = 0$ because of the assumption of fixed ions:

$$\epsilon_0 \vec{\nabla} \cdot \vec{E}_1 = -en_1 \tag{1.9}$$

Let us now introduce the oscillating behavior for the velocity, the electron density and the electron field. Considering for simplicity the 1D scenario we have:

$$\begin{aligned} \vec{v}_1 &= v_1 e^{i(kx-wt)}\hat{x} && (1.10) \\ n_1 &= n_1 e^{i(kx-wt)} \\ \vec{E}_1 &= E_1 e^{i(kx-wt)}\hat{x} \end{aligned}$$

Solving the linearized eq.1.7−1.8 we obtain the angular velocity of the plasma waves:

$$\omega_p = (\frac{n_0 e^2}{\epsilon_0 m})^{\frac{1}{2}} \tag{1.11}$$

Because of the smallness of the mass m, the plasma frequency is usually very high. For a typical electron plasma density $n_e = 10^{18} cm^{-3}$ we have $f_p = \omega_p/2\pi \sim GHz$. These plasma oscillations are also known as Langimuir waves. It is important to underline that ω_p does not depend on k, so the group velocity $d\omega/dk$ is zero: the disturbance does not propagate.

We will now quantify the *high accelerating gradients* that a plasma can sustain. In the linear regime we can write the electron density perturbation as:

$$\frac{\delta n_0}{n_0} \sim \sin(k_p x - \omega_p t) \tag{1.12}$$

If we assume that all the plasma electrons are oscillating with a wave number $k_p = \omega_p/c$, using the Poisson equation, we obtain

$$\epsilon_0 \frac{dE}{dx} = -e\delta n_0 \sim -en_0 \sin(k_p x - \omega_p t) \tag{1.13}$$

The electric field associated to the electron density variation, i.e. plasma oscillations, is then longitudinal with intensity:

$$E \sim e\frac{n_0}{k_p \epsilon_0} \cos(k_p x - \omega_p t) \tag{1.14}$$

Finally it results that plasma can sustain electron plasma waves with electric field of at most

$$E_{max} = \frac{c m_e \omega_p}{e} \tag{1.15}$$

where we have used the definition of the plasma frequency 1.11 and $k_p \sim \omega_p/c$.

Eq.1.15 is referred to as the non relativistic wave breaking field and first derived by Dawson in [3]. For example, a typical plasma density of $n_0 = 10^{18} cm^{-3}$ yields $E_{max} \sim 100$ GeV/m, which is approximately three orders of magnitude greater than that obtained in conventional radio frequency linear accelerators currently limited to ∼100 MeV/m.

Since here we have considered the perturbed plasma, deriving its own responses like the plasma frequency and the arising electrostatic waves. In the next section the accelerating mechanics will be analyzed.

1.1.2 Electromagnetic waves in plasma

Here we derive the characteristics that an electromagnetic wave should have to propagate in a plasma. The derivation is straightforward if we express the fields $\vec{E}$ and $\vec{B}$ and the velocity $\vec{v}$ as a sum of a not perturbed and a perturbed part, indicated with 0 and 1 subscript respectively: $\vec{E} = \vec{E}_0 + \vec{E}_1$, $\vec{B} = \vec{B}_0 + \vec{B}_1$ and $\vec{v} = \vec{v}_0 + \vec{v}_1$. The perturbation is described by the Maxwell equations:

$$\vec{\nabla} \times \vec{E}_1 = -\dot{\vec{B}}_1 \tag{1.16}$$

$$c^2 \vec{\nabla} \times \vec{B}_1 = \frac{\vec{j}}{\epsilon_0} + \dot{\vec{E}}_1 \tag{1.17}$$

where j_1 takes into account the currents due to the charged particles motion. Taking a curl of eq.1.16 and a time derivative of eq.1.17 we have:

$$\vec{\nabla} \times (\vec{\nabla} \times \vec{E}_1) = -\vec{\nabla} \times \dot{\vec{B}}_1 = \vec{\nabla}(\vec{\nabla} \cdot \vec{E}_1) - \nabla^2 \vec{E}_1 \tag{1.18}$$

$$c^2 \vec{\nabla} \times \dot{\vec{B}}_1 = \frac{1}{\epsilon_0} \frac{\partial \vec{j}_1}{\partial t} + \ddot{\vec{E}}_1 \tag{1.19}$$

Assuming a sinusoidal behavior $\sim exp[i(\vec{k} \cdot \vec{r} - \omega t)]$ for the oscillating quantities, for transverse waves it becomes:

$$(\omega^2 - c^2 k^2)\vec{E}_1 = -\frac{i\omega \vec{j}_1}{\epsilon_0} \tag{1.20}$$

If we consider the ions as fixed, the current $\vec{j}_1$comes entirely from the motion of the electrons:

$$\vec{j}_1 = -n_0 e \vec{v}_1 \tag{1.21}$$

where the velocity can be written as

$$\vec{v}_1 = \frac{e\vec{E}_1}{im\omega} \tag{1.22}$$

as obtained from the solution of the linearized electron equation of motion

$$m\frac{\partial \vec{v}_1}{\partial t} = -e\vec{E}_1 \tag{1.23}$$

Eq.1.20 can now be written as

$$(\omega^2 - c^2 k^2)\vec{E}_1 = \frac{n_0 e^2}{\epsilon_0 m}\vec{E}_1 \tag{1.24}$$

The expression for ω_p^2 is recognizable on the right-hand side and the result is

$$k^2 = \frac{1}{c^2}(\omega^2 - \omega_p^2) \tag{1.25}$$

It is clear that for $\omega > \omega_p$ the plasma lets electron pulse to propagate, acting as a nonlinear refractive medium. In this case we have the so called underdense plasma. Conversely, $\omega < \omega_p$ indicates an overdense plasma, in which case the plasma acts as like a mirror. If the plasma response time is shorter than the period of a external electromagnetic field (such as a laser), then this radiation will be shielded out. We conclude deriving the phase and group velocities of the wave traveling through the plasma:

$$v_{ph} = \frac{\omega}{k} = c/\sqrt{1 - \frac{\omega_p^2}{\omega^2}} \tag{1.26}$$

$$v_g = \frac{\partial \omega}{\partial k} = \frac{c^2}{v_{ph}} = c\sqrt{1 - \frac{\omega_p^2}{\omega^2}} \tag{1.27}$$

1.1.3 The dephasing length

In general the electric field of a plasma wave has the form:

$$E_x = E_{max}\sin[\omega_\mathrm{p}(\mathrm{x}/\mathrm{v_p} - \mathrm{t})] \tag{1.28}$$

where $v_p \sim c$ is the phase velocity. The electric field, and thus the electron acceleration, has the same direction as the laser propagation axis. As the electron is accelerated its velocity will increase and approach the speed of light, $v \rightarrow c$. If the phase velocity of the plasma wave is constant with $v_p < v$, the electrons will eventually outrun the plasma wave and move into a phase region of the plasma wave that is decelerating. The condition $v_p >> v$ allows a low energy gain because the particle is too slow with respect to the propagating wave. The optimum condition is to have $v_p \sim v$ so that the electron can be trapped and accelerated.

The limit in the energy gain of the electron in the plasma wave is commonly referred to as electron dephasing. The dephasing length L_d is defined as the length the electron must travel before it phase slips by one-half of a period with respect to the plasma wave. It is:

$$k_p(L_d - v_p t) = \pi \tag{1.29}$$

and assuming a highly relativistic electron $v \sim c$ we have:

$$(1 - \frac{v_p}{c})L_d = \frac{\lambda_p}{2} \rightarrow L_d \sim \gamma_p^2 \lambda_p \tag{1.30}$$

The maximum energy gain after a dephasing length is:

$$W_{max} = eE_{max}L_d \sim 2\pi\gamma_p^2 m_e c^2 \tag{1.31}$$

A reasonable number for the maximum energy gain, considering a fully relativistic propagation with $\lambda_p = 100\mu m$ and $L_d = 1m$ is $\Delta W_{max} \sim 30GeV$.

1.1.4 The normalized vector potential

Before pointing the attention to the expression of the accelerating force, we have to introduce a useful quantity for the following. The normalized vector potential defined in terms of the potential vector $\vec{A}$ of the electromagnetic field is defined as:

$$\vec{a} = \frac{e\vec{A}}{m_e c^2} \tag{1.32}$$

and related to the laser intensity I_0 through:

$$a^2 = 7.3 \times 10^{-19}[\lambda(\mu m)]^2 I_0(W/cm^2) \tag{1.33}$$

This parameter sets a boundary between linear and relativistic behavior. Considering the not relativistic case we can write the equation of motion of the electron as:

$$\frac{\partial \vec{v}}{\partial t} = -\frac{e\vec{E}}{m_e} \tag{1.34}$$

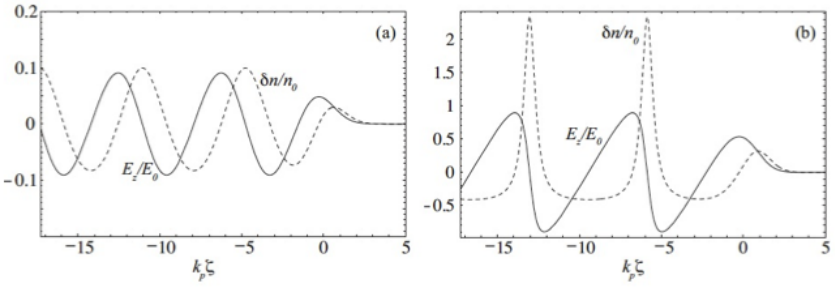

Figure 1.1. Electron density perturbation (dashed line) and plasma wave electric field (solid line) excited by a Gaussian laser pulse with normalized intensity $a = 0.5$ (on left) and $a = 2.0$ (on right) .

The solution expressed in terms of the potential vector is:

$$\vec{v} = \frac{e\vec{A}}{cm_e} \tag{1.35}$$

Using the definition in eq.1.32, we find $v/c = a$ that justifies the linear not relativistic description when $a < 1$. Fig.1.1 shows the solutions for the two situations: the linear, perfectly sinusoidal, and the relativistic response of the electron density to the propagation of a Gaussian laser beam are shown on the left and on the right respectively.

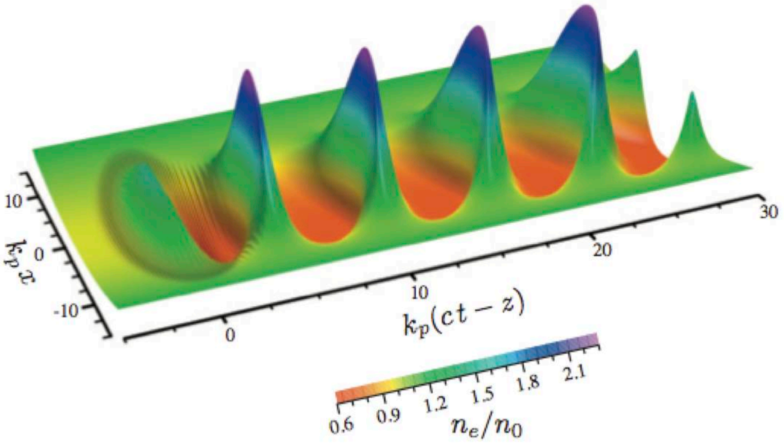

Figure 1.2. Plasma density perturbation excited by a Gaussian laser pulse with $a = 1.5$. Laser pulse is traveling to the left.

Fig.1.2 shows an example of a nonlinear plasma wave in a two-dimensional simulation, as computed using a fluid model. The density perturbation is excited by a Gaussian laser pulse with $a = 1.5$.

1.1.5 The ponderomotive force

In laser plasma acceleration electrons are pushed forward by the ponderomotive force. A simple way to derive its expression is to consider the electron fluid momentum equation in the linear limit $|a| = e|A|/m_e c^2 \ll 1$:

$$\frac{d\vec{p}}{dt} = -e[\vec{E} + \frac{1}{c}(\vec{v} \times \vec{B})] \tag{1.36}$$

where $\vec{p}$ and $\vec{v}$ are the electron momentum and velocity, respectively. The electric and magnetic field of the laser can be written as

$$\vec{E} = -\frac{1}{c}\frac{\partial \vec{A}}{\partial t}, \qquad \vec{B} = \vec{\nabla} \times \vec{A} \tag{1.37}$$

in terms of the vector potential of the laser $\vec{A}$. Letting $\vec{p} = \vec{p}_q + \delta\vec{p}$, we derive:

$$\begin{aligned}
\frac{d\vec{p}}{dt} &= \frac{\partial \vec{p}_q}{\partial t} + (\vec{v} \cdot \vec{\nabla})\vec{p}_q + \frac{d\delta\vec{p}}{dt} && (1.38)\\
&= -e[-\frac{1}{c}\frac{\partial \vec{A}}{\partial t} + \frac{1}{c}(\vec{v} \times \vec{\nabla} \times \vec{A})] && (1.39)\\
&= mc\frac{\partial \vec{a}}{\partial t} - mc\vec{v} \times \vec{\nabla} \times \vec{a} && (1.40)
\end{aligned}$$

At the first order it clearly emerges the definition of the quiver momentum $\vec{p}_q = m_e c\vec{a}$. Solving the second-order motion we find the expression of the ponderomotive force in the linear regime ($a^2 \ll 1$):

$$\begin{aligned}
\frac{d\delta\vec{p}}{\delta t} &= -[\frac{1}{m_e}\vec{p}_q \cdot \vec{\nabla}]\vec{p}_q - c\vec{p}_q \times \vec{\nabla} \times \vec{a} && (1.41)\\
&= -m_e c^2 \frac{\vec{\nabla} a^2}{2} && (1.42)
\end{aligned}$$

This is an effective non linear force on a single electron. If we consider the electron density n_0 in terms of ω_p^2 we obtain the ponderomotive force proportional to:

$$\vec{F}_p \sim -\frac{\omega_p^2}{\omega^2}\vec{\nabla} E^2 \tag{1.43}$$

It results to be proportional to the laser intensity and to the electron density, being $\omega_p \sim n_e^{1/2}$. So the electrons are pushed away from the high density region and this density perturbation leads to an electron wave creation on the wake of the laser.

Fig.1.3 shows the mechanism through which the ponderomotive force excites the electron waves.

1.2 The acceleration configurations

There are different experimental configurations for plasma based accelerators. The most widely investigated are:

- Plasma-based accelerators (PWFA) in which the plasma is driven by one or more electron beams. In this configuration, plasma wakefield can be excited by a relativistic electron beam provided that the electron beam is shorter that the plasma period;

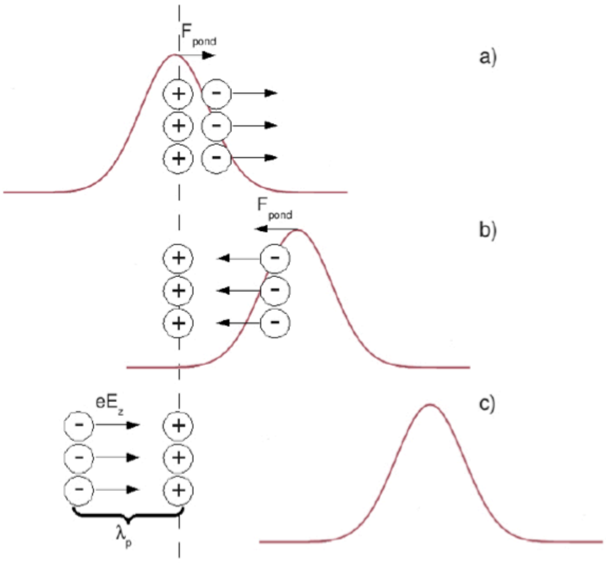

Figure 1.3. Ponderomotive force action: the laser is traveling from left to right, the electrons are pushed forward and start to oscillate around the ions assumed to be at rest.

- Plasma beat-wave accelerators (PBWA) where two long pulse laser beams of frequencies ω_1 and ω_2 are used to resonantly excite a plasma wave. This is done by appropriately adjusting the laser frequencies and plasma density such that the resonance condition $\omega_1 - \omega_2 = \omega_p$ is satisfied;
- Laser wakefield accelerators (LWFA) in which a single short ($\leq$1 ps) ultrahigh intensity ($> 10^{18}$ W/cm^2) laser pulse drives a plasma wave. The wakefield is driven most efficiently when the laser pulse length $L = c\tau_L$ is approximately the plasma wavelength $\lambda_P = 2\pi c/\omega_P$, i.e. $L \sim \lambda_P$.

Our attention is focused on the LWFA because this is the scheme used in the PlasmonX experiment.

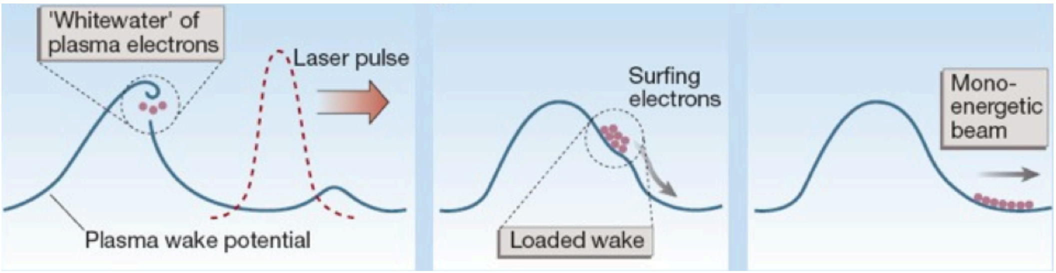

Figure 1.4. Schematic view of the wave breaking mechanism.

In this configuration the laser pulse leaves behind its passage (on the laser wake) a plasma wave. Fig.1.4 shows the highly non linear process called wave breaking. The wake potential rises until it steepens and breaks. Electrons from the plasma are caught in the 'whitewater' and surf the wave. The load of the electrons deforms the wake stopping further trapping of electrons from the plasma. As the electrons surf to the bottom of the wake potential, they each arrive bearing a similar amount of energy [6].

Another less investigated mechanism is the so called external injection. Once the electron plasma wave is created (for example through the laser pulse propagation), external pre-accelerated electrons can be injected in the plasma waves. This leads to a greater energy gain and is the first step towards the multi-stage scheme based on a succession of laser-plasma accelerators. The synchronization is a crucial aspect.

1.3 Historical overview of the experimental results

A decade of experiments (1994-2004) demonstrated the feasibility of this new accelerating technique. They have demonstrated acceleration gradients >100 GeV/m, accelerated electron energies >100 MeV, and accelerated charge >1 nC. The weak point was the quality of the accelerated electron bunches: typically the accelerated bunch was characterized by an exponential-Boltzmann like energy distribution, with most of the electrons at low energy (<10 MeV) and a long exponentially small tail extending out to high energy (>100 MeV). Although the bunches had large energy spread, they were typically well collimated with divergences less then 10 mrad [7].

Typically the energy measurements are done deflecting the particles through a magnet and detecting their final position by a phosphor screen (see fig.1.5). The response of the phosphor screen consists in the number of counts on the CCD vs deposited charge, normally calibrated against the ICT counts. There are several advantages in using this optical devices mainly because of the extremely small position resolution and the two dimensional information. The weak aspects arise because they are: difficult to read for large areas and sensitive to radiations. The linearity for very high charge is not been demonstrated.

As an example we show in fig.1.6 results from Lawrence Berkeley National Laboratory group [8]. Preliminary spectral measurements indicates that bunches as short as 30-50 fs have been produced in these laser driven accelerators.

1.3.1 High quality bunch production at the 100 MeV level

More interesting results come out after 2004 when three important facilities demonstrated, independently, the possibility to produce high quality electron bunches. This resulted from a higher degree of control of the laser and plasma parameters, an improvement of diagnostic techniques, an extension of the laser propagation distance through the plasma, and a greater understanding of the underlying physics, in particular, the importance of matching the acceleration length to the dephasing length.

- the group located at the Rutherford Appleton Laboratory (RAL) in the United Kingdom used 0.5 J, 40 fs laser pulse focused on a 2 mm long gas jet with

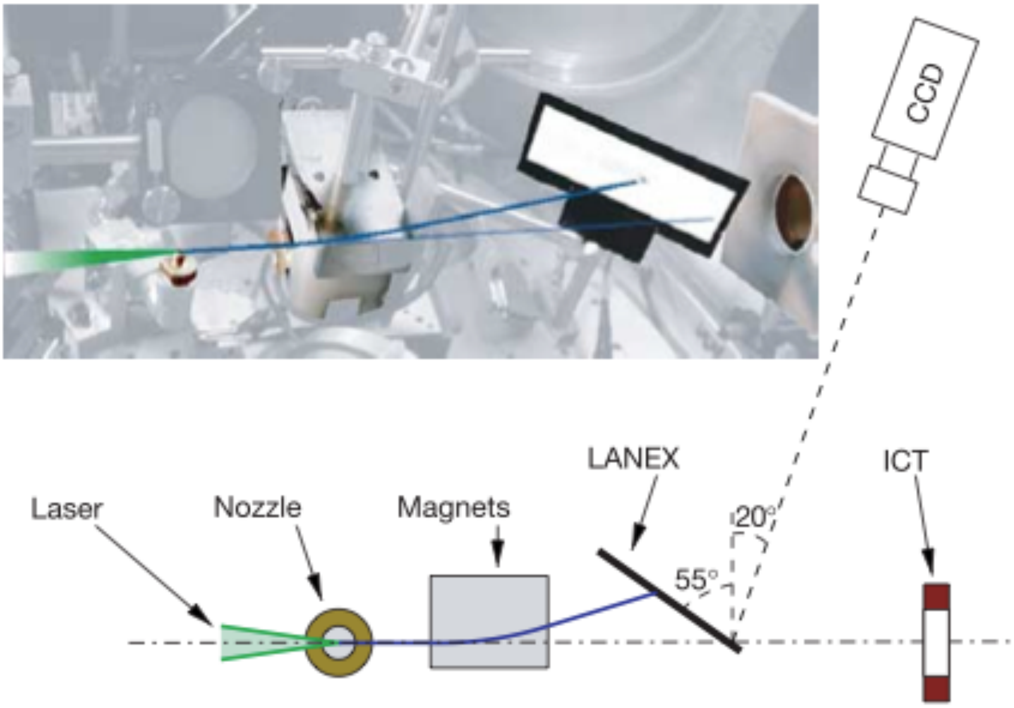

Figure 1.5. Typical experimental set-up in laser plasma acceleration experiments, picture and diagram. An ultrashort and ultraintense laser pulse is focused onto a supersonic gas jet and produces an electron beam. In the diagram is well visible the LANEX-a phosphor screen, the CCD-charge-coupled device camera and the ICT-integrating current transformer.

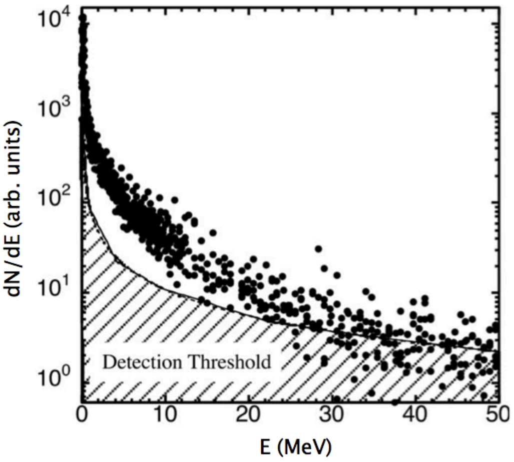

Figure 1.6. Electron energy spectrum measurement. The spectrum was obtained by scanning the excitation current in the magnet and measuring the intensity on a phosphor screen. Each data point represents 10 shots. The spectrum is reasonably well approximated by a Boltzmann distribution with an effective temperature of 4.6 MeV.

a plasma density of $2 \times 10^{19} cm^{-3}$. A bunch with narrow energy spread was observed at 78 MeV with 3% FWHM energy spread, 22 pC of charge [9].

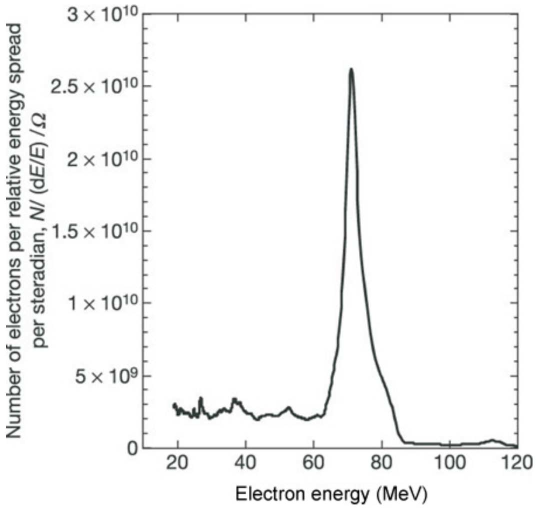

Figure 1.7. Measured electron spectrum. The energy spread is ±3%, with a fluctuation of the mono-energetic beam ~30%, owing to variations of the laser parameters.

Fig.1.7 shows a clear mono-energetic signal. For shots with the lowest energy spread (<10%) the beam energy varied between 50 and 80 MeV. This is due to shot-to-shot variations in the laser parameters.

- the group located at the Laboratoire d'Optique Appliquee (LOA) in France used a 1 J, 33 fs laser pulse focused on a 3 mm gas jet with a plasma density of $6 \times 10^{18} cm^{-3}$. A narrow energy spread bunch was ob-served at 170 MeV bunch with a 24% energy spread, divergence of 10 mrad FWHM, and 500 pC of charge.

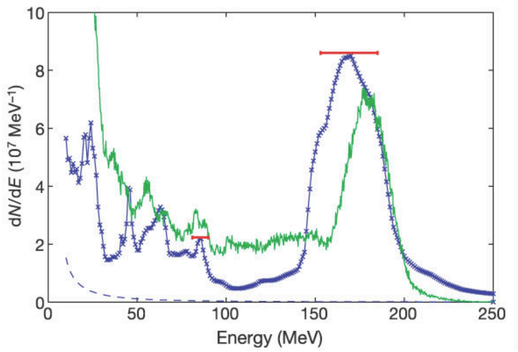

Figure 1.8. Energy spectrum is shown in blue line with crosses. In green is shown the electron spectrum obtained from 3D PIC simulations. Red horizontal error bars is the resolution of the spectrometer.

Fig.1.8 shows the experimental and the simulated electron spectra.

- the group located at the Lawrence Berkeley National Laboratory (LBNL) in the United States operated with preformed plasma channels, created using additional laser pulse, with an on-axis density of $2 \times 10^{19} cm^{-3}$. Guiding of high-intensity laser pulses in plasma channels is necessary in order to extend the acceleration length, and thus the energy gain. The experiment used to guide a 9 TW, 55 fs laser pulse, focused on 8.5 μm spot size to reach the intensity of $10^{19} W/cm^2$ through the 2 mm gas jet. Bunches containing 2×10^9 electrons at 86 MeV with a 3.6 MeV energy spread were observed with a divergence near 3 mrad [10].

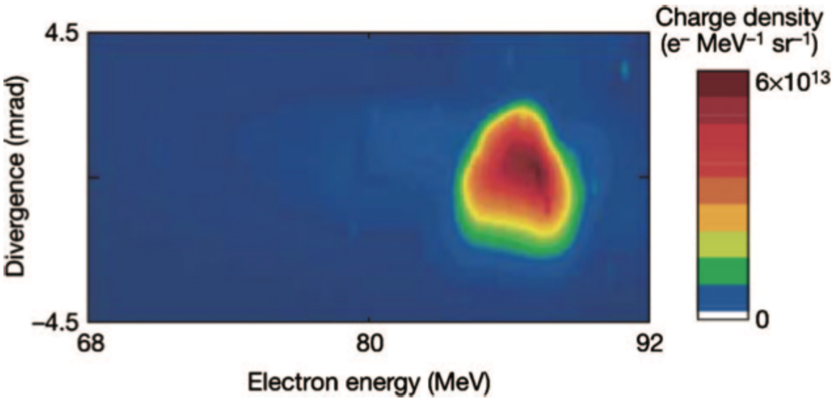

Figure 1.9. Electron energy spectrum of the channeled acceleration.

Fig.1.9 shows the electron energy spectrum of a bunch produced by the channel-guided LWFA. Due to pointing fluctuations which change the in-coupling of the drive beam to the guide, this feature varied shot to shot, and bunches with 3×10^9 electrons at 78 MeV were observed, as well as 1×10^9 electrons at energies up to 150-170 MeV.

1.3.2 High quality bunch production at the 1 GeV level

To reduce the energy spread of the accelerated electron bunches a technique based on capillary was developed: structures with micrometric diameter (used instead of the gas jet) to guide the laser and to limit the diffraction effects. In experiments at LBNL a gas-filled capillary discharge waveguide was used to produce centimeter scale lower density plasma channels. The experiments used a 40 fs laser pulse with up to 40 TW peak power. These pulses were focused at the capillary entrance, with an input intensity of $10^{18} W/cm^2$ [11], [12].

The capillaries were 33 mm long sapphire blocks with diameters ranging from 190 to $310 \mu m$. Hydrogen gas, introduced through two holes near the capillary ends, was ionized by striking a discharge between electrodes at the capillary ends, producing a plasma channel. Accelerator performance was optimized by adjusting the initial gas density and the delay between onset of the discharge current and arrival of the laser pulse (from 1.0×10^{18} to $4.0 \times 10^{18} cm^{-3}$ in an $\sim 100 ns$ timing window).

Fig.1.10 shows energy spectra of electron bunches produced at 0.5 GeV with $\sim$ 50 pC charge and at 1.0 GeV with 30 pC charge, obtained using 12 TW , 73 fs input, and 40 TW, 38 fs input, laser pulses, respectively. In both cases the electron bunches had percent-level energy spread and divergence of $1.2-2.0$ mrad.

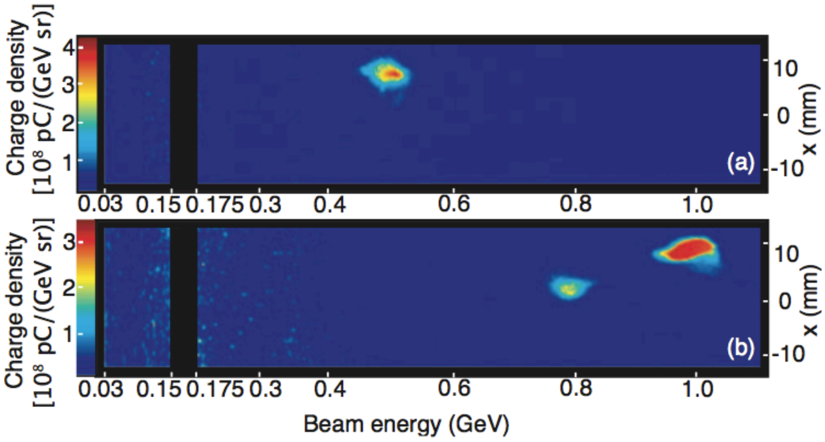

Figure 1.10. Single-shot electron bunch spectra of the capillary-guided LWFA.

Chapter 2

The PlasmonX project and SITE experiment

2.1 General layout of the project

The aim of the PlasmonX project is to provide the Laboratori Nazionali di Frascati (LNF) with a world-class, high-power laser facility suitable for multidisciplinary experiments that have roots in particle physics, quantum optics and applied physics fields [13].
The main purpose of the facility will consist in R&D activity aimed at:

- demonstrate the high-gradient acceleration technique by the use of ultra-short, high power laser pulses;
- develop a monochromatic and tunable X-ray source in the 20-1000 keV range, based upon Thomson Scattering of laser pulses by relativistic electrons.

The strategic position of the facility, built in close interaction with the SPARC project−a high brightness electron beam source [14], will give the possibility to operate also experiments of external injection: for the first time the possibility to inject pre-accelerated electrons into electron plasma waves excited by the laser pulses will be explored. A solution proposed to improve the parameters of the electron beam, and thus to make possible the realization of a high quality accelerator based on laser-plasma interaction, is to use a more powerful laser system and to use a multi-stage acceleration scheme based on a succession of laser-plasma accelerators In order to establish the performances of the laser system and of the diagnostics a Self Injection Test Experiment (SITE) has been planned [15]. It deals only with the self-injection.

Fig.2.1 shows the experimental set-up of SITE and the related optical diagnostics. The optical diagnostic consists in Thomson scattering images that detect the electromagnetic radiation scattered by the electrons. Thomson Scattering from free electrons is a pure electrodynamic process in which each particle radiates while interacting with an electromagnetic wave. From the quantum-mechanical point of view Thomson scattering is a limiting case of the process of emission of a photon by an electron absorbing one or more photons from an external field, in which the

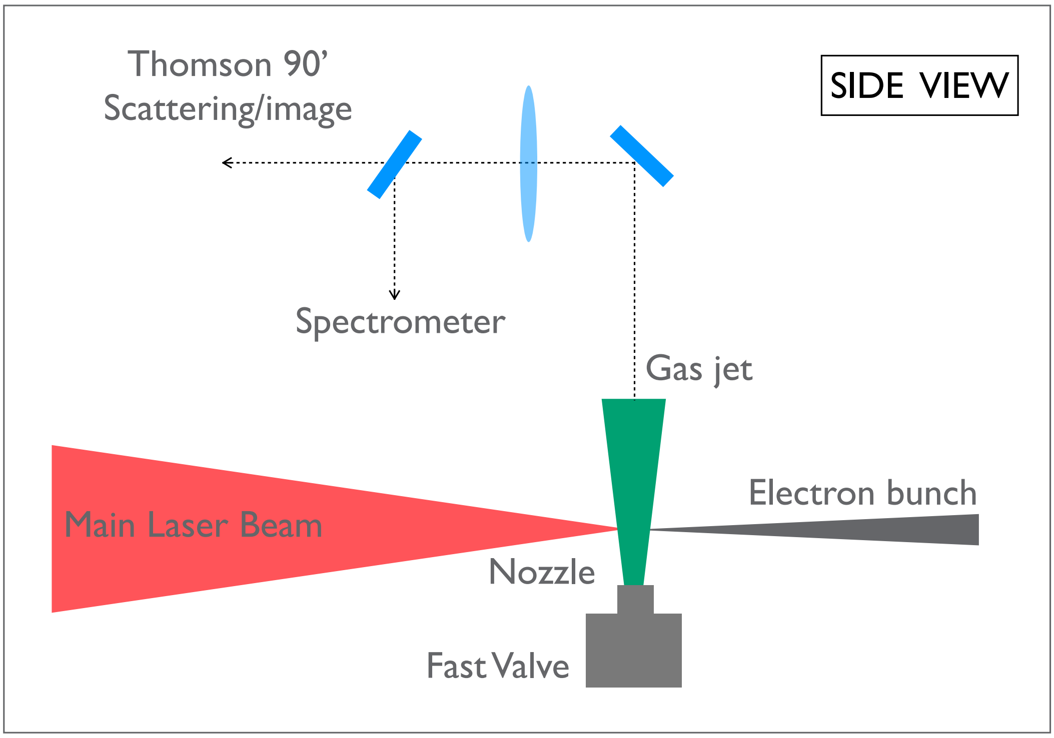

Figure 2.1. Schematic set-up of the Self Injection Test Experiment.

energy of the scattered radiation is negligible with respect to the electron’s energy. The scattering is described by an emission coefficient ϵ which is defined as

$$\epsilon = \frac{\pi \sigma_T}{2} I n_e \cos^2 \chi \tag{2.1}$$

where σ_T is the Thomson cross section for the charged particle, n_e is the density of charged particles at the scattering point, I is the incident flux and χ is the angle between the incident electric field and the observer.

The Thomson images are also used to study the focalization length of the laser pulse and the plasma acceleration length.

The accelerated electrons propagate in vacuum, are deflected by a magnetic dipole and impact the position detector. The accelerated electrons are deflected by a dipole and then detected by an electron spectrometer for the beam characterization. This device will be largely discussed in the next two chapters.

2.1.1 The laser FLAME for the acceleration

FLAME (Frascati Laser for Acceleration and Multidisciplinary Experiments) is a new and high performance laser source designed by Amplitude Technologies. The 250 TW laser system is a compact femtosecond laser source providing more than 7.5 J pulse energy at 10 Hz repetition rate. The pulse length is about 22 fs and leads to a peak power higher than 250 TW with an average power of ~75 W.

The system is a Titanium-Sapphire laser based on the so-called *Chirped Pulse Amplification* (CPA) scheme [16]. It consists of a full integrated Ti:Sa oscillator with its DPSS (Diode Pumped Solid State) pump laser, a stretcher, a regenerative amplifier, two multi-pass amplifiers pumped by three Nd:YAG lasers and a vacuum compressor. Fig.2.2 shows the different stages of the CPA technique.

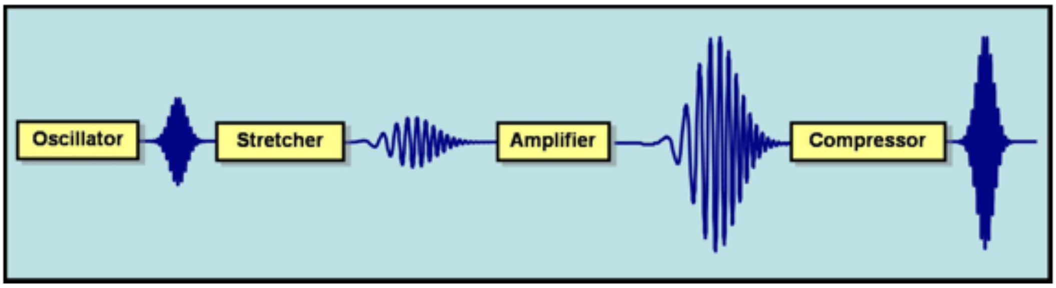

Figure 2.2. Principle of Chirped Pulse Amplification.

The most important characteristics of the components of the system are here detailed:

- the Ti:Sa oscillator generates pulse durations from sub-10 to sub-20 fs with an operational rate of 80 MHz. It is a commercial *Synergy* manufactured by *Femtolasers* and delivered with its own pump laser.
- the booster is important to improve contrast ratio up to $10^9 - 10^{10}$. This module consists in a compact amplifier to amplify the oscillator output up to the μJ level.
- the stretcher is used in the first step of the CPA technique: the principle is to create different optical paths for each wavelength by means of dispersive systems as gratings. An amplified femtosecond pulse has an enormous peak power, up to 100 TW, so temporally stretching the pulses before amplification is required to prevent damage to the amplifying medium and other optical components in the amplifier. A pair of gratings disperses the spectrum and stretches the pulse by a factor 10^3 (see fig.2.3). As it can be seen in fig.2.3, the blue path is longer than the red one. Therefore, blue wavelengths take more time to travel through the system than red ones. Due to Fourier transform properties, a femtosecond pulse exhibits a broad spectrum (typically 26 nm for a 30 fs pulse). Since the bluer part of the spectrum is delayed compared to the redder part when traveling through the stretcher, the output pulse is stretched and looks like a temporal rainbow (red in the leading edge and blue in the trailing edge). The stretching factor depends on the spectral width of the input pulse and on the intrinsic characteristics of the stretcher (grooves density of the gratings, distance between the gratings, number of roundtrips in the stretcher, incidence angle, etc...). For a given stretcher configuration, the wider the input spectrum is, the longer the stretched pulse is.
- the amplifier stages are: a regenerative amplifier followed by a 5-pass amplifier then a 4-pass amplifier and the main amplifier which is a 3-pass. The first

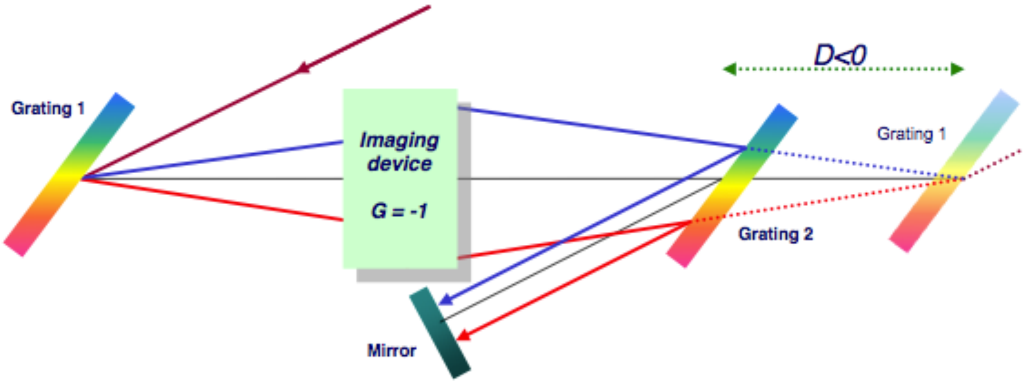

Figure 2.3. Pulse stretcher using two wavelength dispersing diffraction gratings: the principle is to create different optical paths for each wavelength of the spectrum. The stretching factor depends on the distance D between the two gratings.

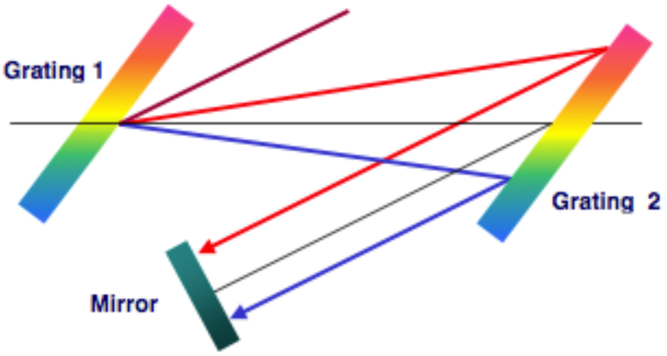

Figure 2.4. Principle of a pulse compressor.

amplification stage produces around 1 mJ stretched pulses at 10 Hz. Then the energy is progressively raised to 25 mJ, 600 nJ and up to 7 J. At the output of the amplifying system the energy does not depend on the input pulse duration delivered by the oscillator.

- the vacuum compressor is used to compress back the pulse to its initial duration. A compressor device based on a wavelength dispersion system very similar to the stretcher is used (see fig.2.4). After the compression stage, one obtains a high intensity ultra short pulse.

The laser system is realized on two levels: the clean room where the laser is generated in air and an underground target area (bunker) where the vacuum compression takes place. The bunker also hosts the interaction vacuum chamber, the optical diagnostics and the electron spectrometer for the energy beam characterization.

Table 2.1. Input values used in the PIC simulation.

$L_{gas-jet}$ [mm]	n_e $[cm^{-3}]$	τ [fs]	I_0 $[W/cm^2]$	ω_0 [μm]
4	4×10^{18}	30	5.3×10^{19}	13

2.1.2 The target area

Once the laser is fully amplified, it is sent down in the bunker (or target area, see fig.2.5) thanks to optical mirrors that guide the laser beam inside the vacuum compressor. After the time compression it is focalized, using a off-axes parabola, onto the gas-jet placed inside the interaction chamber. The pressure inside the chamber is $\sim 10^{-6}$ mbar. We use a rectangular gas-jet nozzle – dimensions 10×4 mm – and we fire the laser perpendicularly to the long edge (see fig.2.6). The shape of the nozzle (de Laval) is been studied in order to give a supersonic gas-jet and provide a steep vacuum-plasma separation surface. The plasma density can be varied changing the backing pressure of the gas.

The vacuum chamber is provided with 13 optical windows, 8 of which are on the top and allow the optical diagnostics placement. A first qualitatively characterization of the laser-plasma interaction comes from the Thomson scattering observed normally to the electron oscillation direction.

The electron diagnostic consists of the electron spectrometer I collaborated to design and realize, together with the group of Rome. The main idea is simply the following: once the electron bunch is produced it propagates in vacuum so to reduce the multiple scattering effects. A magnetic field can be used to obtain an energy depending trajectory and a position detector to measure the final deflection. The following chapters will describe in details the work done. But before that we have to characterize the expected accelerated electrons beam: after this last section it would be clear where the challenge is.

2.1.3 Expected spectra of the accelerated electrons

Even if the basic physical phenomena of the laser-plasma interaction are understood and formalized in the Maxwell-Vlasov equations describing the fields propagation and the particles evolution, a complete 3D relativistic treatment which deals with experiments requires a numerical approach. In the framework of PlasmonX collaboration the relativistic PIC code ALaDyn (Acceleration by Laser and dynamics of charged particles) has been developed at the Department of Physics of the Bologna University.

Considering the experimental parameters of SITE, summarized in tab.2.1, a fully self-consistent 3D PIC simulation has been performed using the ALaDyn code. Simulation results are summarized in fig.2.7: it shows the evolution of the electron density, i.e. the formation of the bubble and the accelerated bunch, and the energy spectrum as a function of time. At the end of the propagation (ct=4.0 mm) a bunch with a peak energy of 0.9 MeV is out-coming. The energy spectrum is also characterized by a broad tail at low energies: we observe that the whole bunch,

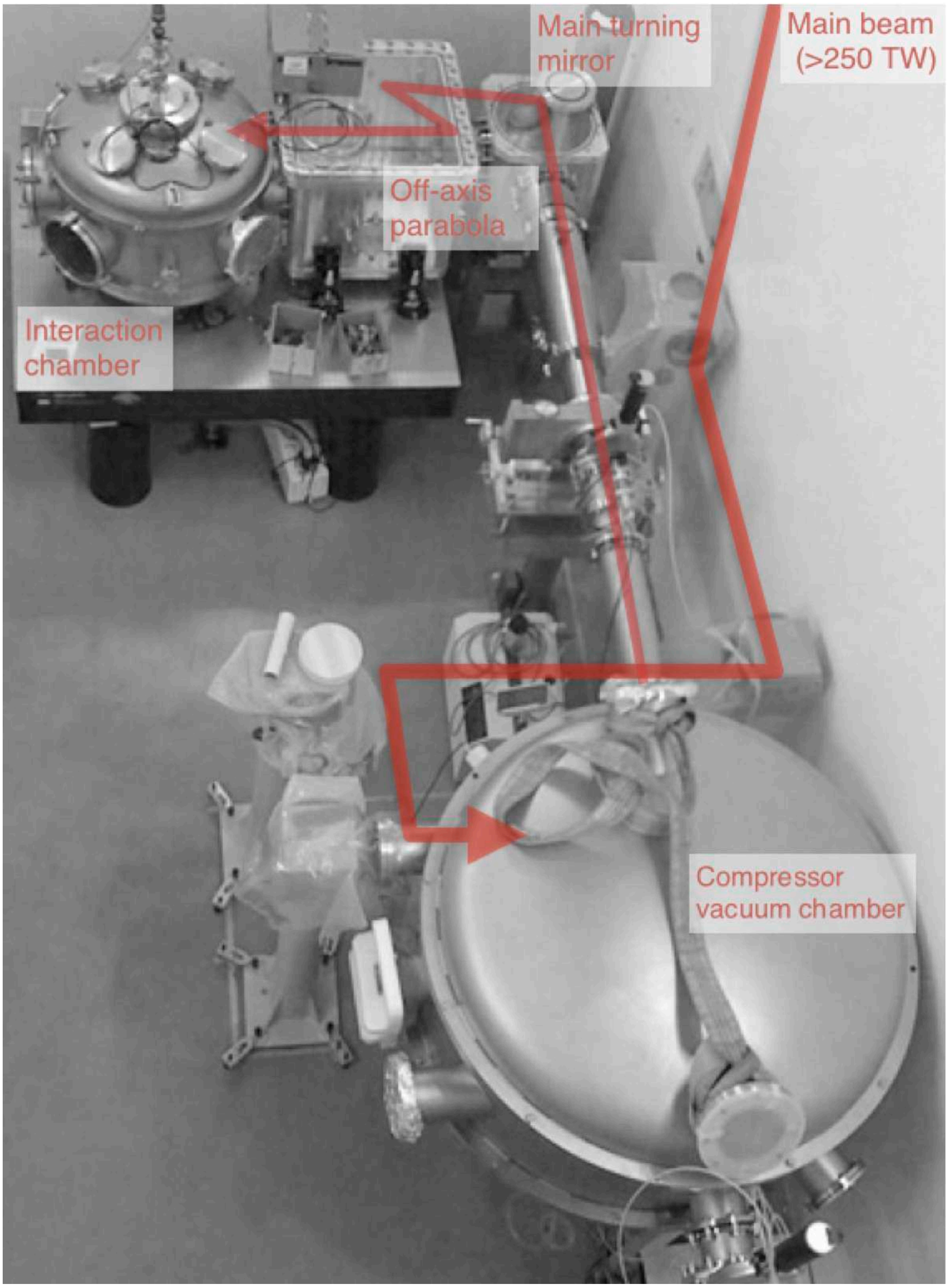

Figure 2.5. Main devices present in the bunker area.

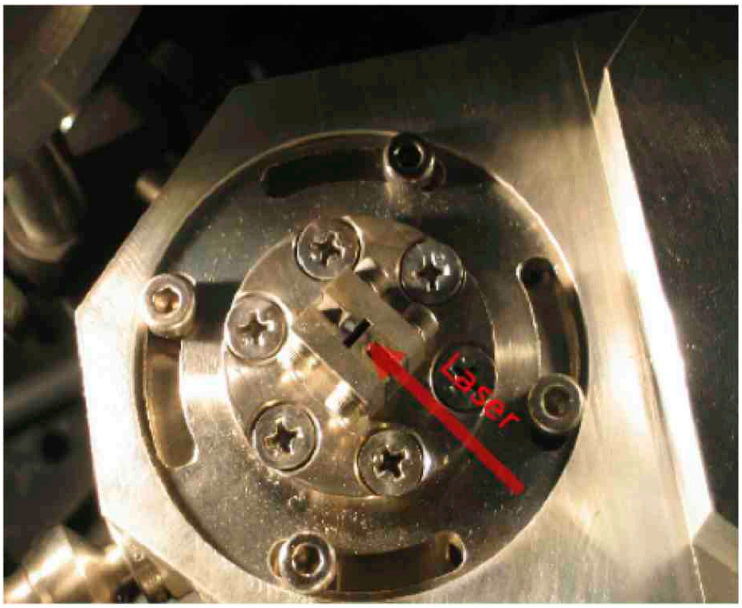

Figure 2.6. Top view of the gas-jet, dimensions 4 × 1.26 mm. The laser is fired perpendicularly to the long edge.

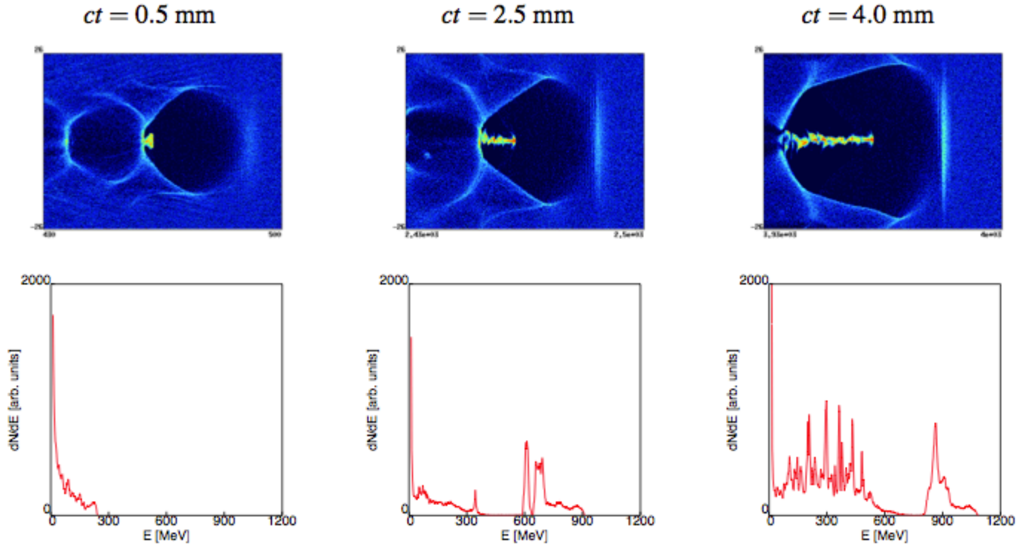

Figure 2.7. Electron density (top line) and energy spectrum (bottom line) at different times in the 3D PIC simulation for the SITE experiment.[17]

which needs to be detected in order to characterize the accelerated bunch produced, has an energy spread over three order of magnitude. The charge of the high energy structure is calculated to be 0.6 nC: the number of the accelerated electrons is $\sim 10^{10}$. The bunch length is 1.8 μm (which means an extremely short bunch of 6 fs).

Another important observation arises considering the plot in fig.2.8: the expected

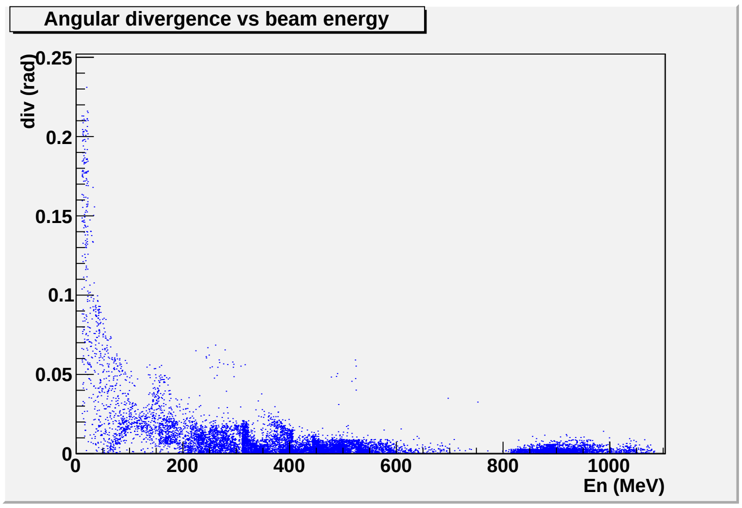

Figure 2.8. Expected angular dispersion distribution.

angular dispersion distribution is strongly correlated with the bunch energy and only the high energy structure is collimated in few mrad.

Experimentally such a kind of bunch is hard to be analyzed using conventional particle detectors mainly because of three reasons: the huge number of electrons impacting at the same time the detector, the very broad energy spread and the unknown initial angular divergence.

In the following chapter it will be clear how we have dealt with these peculiar characteristics, the problems arisen and the solutions proposed.

Chapter 3

Design and realization of the magnetic spectrometer of SITE

Having introduced the PlasmonX project and the SITE experiment in the previous chapters, this one is focused on the device I collaborated to realize during my PhD. In this chapter the magnetic spectrometer is analyzed in every single component. To reconstruct the energy spectrum of the accelerated electrons we deflect the particles with a dipole and perform a position measurement. Both the magnet and the detector are described in the first section of this chapter. In the second section we define the data analysis procedure. The chapter ends with the simulation of what signals we expect to observe on the detector.

To complete the discussion, the next chapter will describe the performance of the device.

3.1 Global design

The detector designed for SITE [15] experiment represents a challenge for all the fields it involves. To work with a huge number of particles arriving simultaneously at the detector is unusual in the high-energy field; the GeV energy region is still not-explored from the laser-plasma field and the accelerator physics deals with extremely smaller emittances.

In order to measure the electron energy spectrum we propose the general layout shown in fig.3.1. The electrons accelerated by the laser propagating in x direction will traverse a region where a vertical magnetic field is present and will therefore have a momentum-dependent deflection in the y direction. The measurements of the position of such particles on appropriately shaped detectors allows the measurement of the momentum.

The electron bunch suffers of a divergence (see fig.2.8) depending on the energy, and only the high energy peak is collimated within few mrad. The electron source is a point-like spot located more then a meter before the region with magnetic field. Finally, due to the possible low energy of the particles of interest, the beam needs to be kept in vacuum. The choice therefore falls on electromagnets with a vacuum

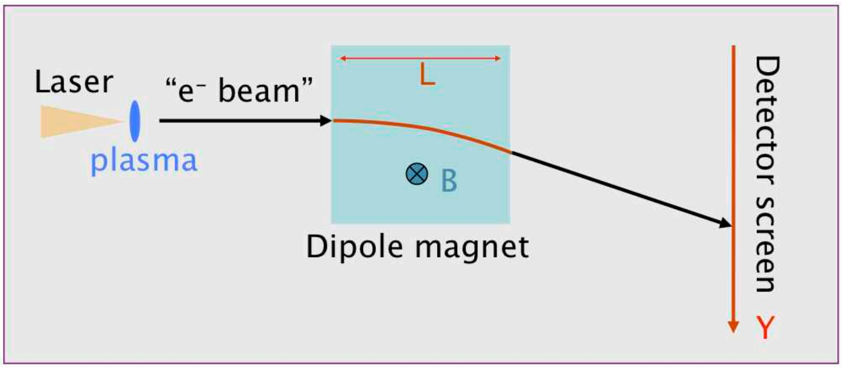

Figure 3.1. General layout and reference system: the electrons accelerated in x direction are deflected by a vertical magnetic field and deflected in y direction.

pipe within the magnetic dipole gap.

The need to build a first working device in short terms forced us to use spares of past experiments. The spectrometer is made of a magnet spare from LISA, scintillating fibers from NA62 and electronics developed by the Instituto Superiore di Sanita' of Rome. The design had also to cope with stringent space constraints, as the room allocated to the diagnostics was fixed before the activity started.

3.1.1 Dipole characterization and focusing property

The shape of the magnetic field and the location of the position detectors are dictated by the need to minimize the resolution on the momentum for a fixed resolution on the position coordinate. While the optimal dispersion can be achieved by positioning the detectors as far as possible, this is not necessarily the optimal criterium for an electron beam produced in laser-plasma acceleration experiments. The momentum resolution is in fact dominated by the angular dispersion which overlays in a given position trajectories from significantly different momenta.

This component of the error can be shrunk if there exist focii of the trajectories, i.e. points where all trajectories of a given momentum converge regardless of the angle at the origin.

In the SITE experiment we operate with a spare dipole that is not the optimized one: after a brief characterization of the magnetic field, it will be shown how to operate with such a device in order to obtain the better possible energy focalization.

The bending dipole in use is shown in fig.3.5. The only parameters important for the following are the pole gap of 6 cm and the maximum induction of 0.5 T. The device operates if supplied with 23 V with current 103 A. The water flow is 1.7 l/min. The pole extension is 18 cm. The magnet is provided with two interlock systems: one for the water flow and one for the temperature rise.

Fig.3.6 shows the measured magnetic field B_z as a function of the applied current: the working point is at 100 A with induction 0.5 T.

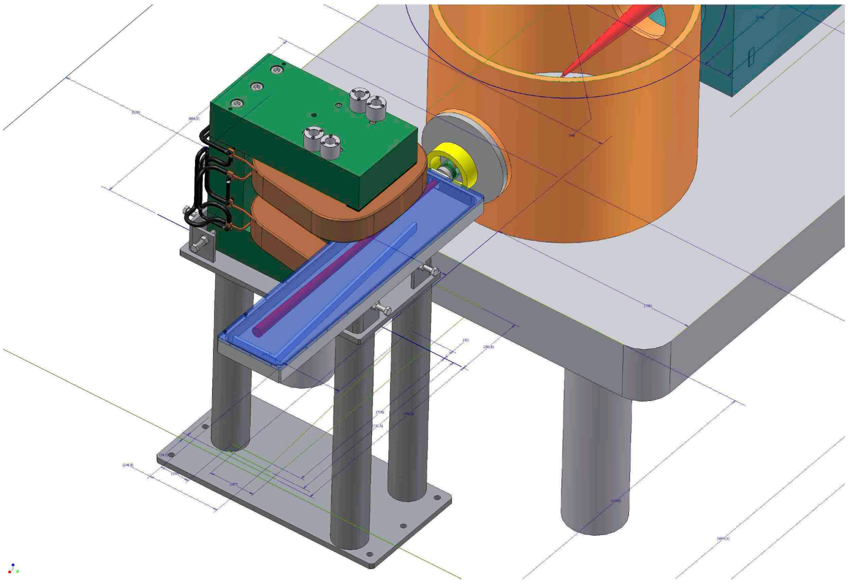

Figure 3.2. CAD image of the electron spectrometer: the detector is inside the vacuum pipe placed within the magnetic dipole gap.

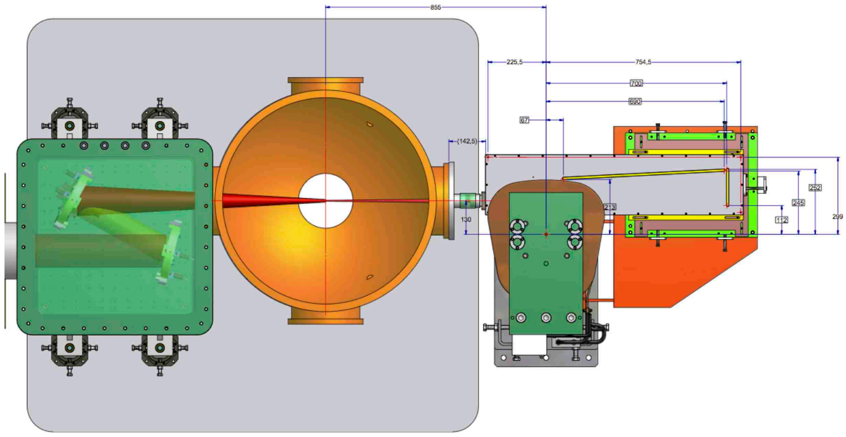

Figure 3.3. Encumbrances of the experimental area.

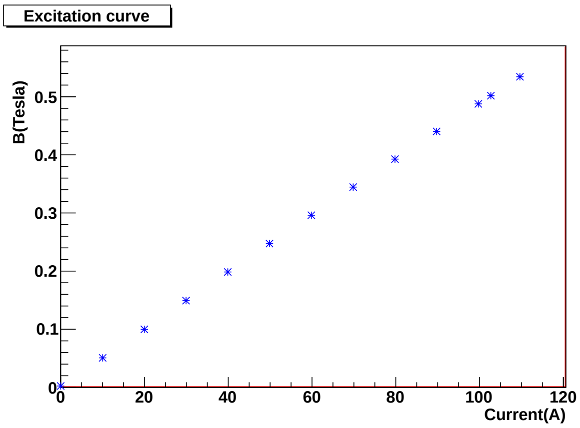

Figure 3.4. Excitation curve for the magnetic dipole: the working point is at 100 A with 0.5 T induction.

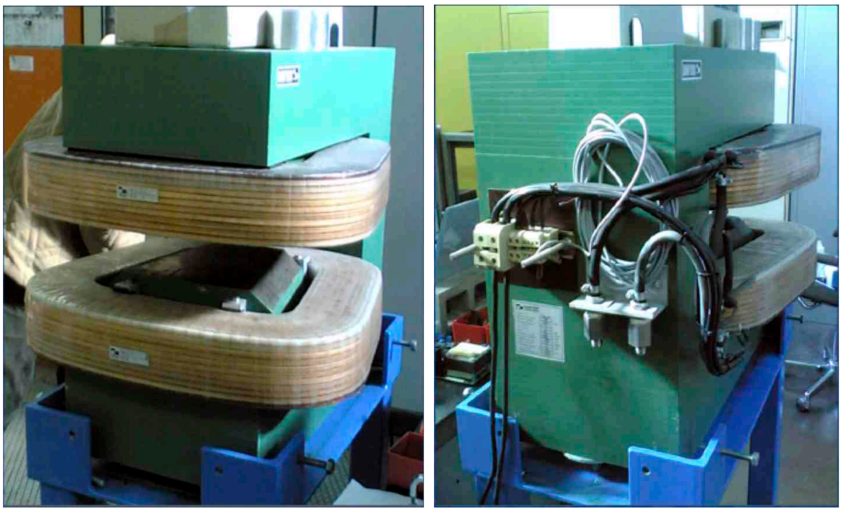

Figure 3.5. Magnetic dipole in use.

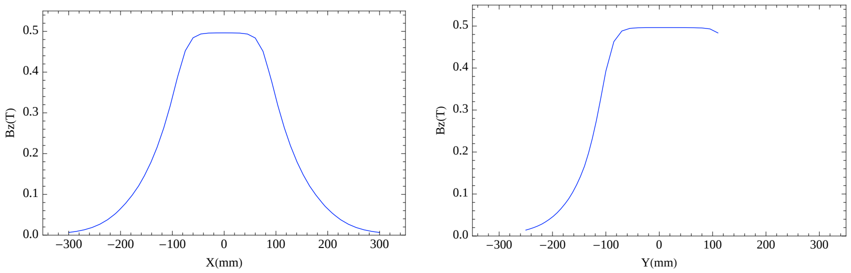

Figure 3.6. Magnetic field profile along x(left) and y(right) directions.

The magnet field is measured in three planes using a Hall probe: at $z = \pm 12$ mm and z=0 mm. For a fixed z, steps in y direction are regularly taken every 10 mm from $y = -250$ mm to $y = 110$ mm; in x direction Bz was measured from $x = -300$ mm to $x = 300$ mm with steps of 15 mm. The grid is linearly interpolated between measured point and a $3D$ profile is shown in fig.3.7.

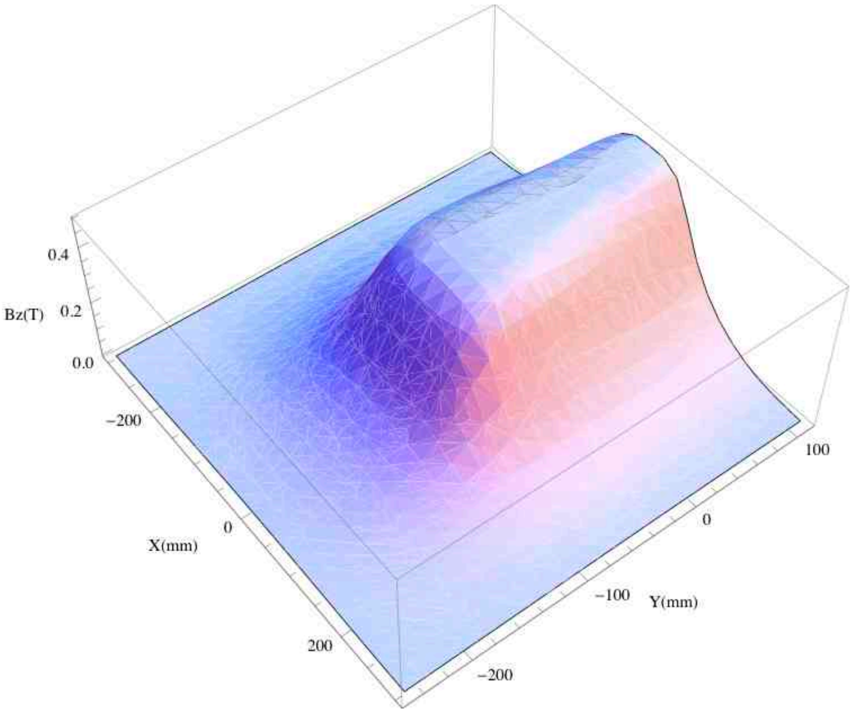

Figure 3.7. Magnetic field in the pole region.

In principle in order to measure energies over a broad range we have to maximize the deflection of the beam. The magnetic field is not negligible even outside the dipole region. For this reason, a useful quantity to study the beam deflection is given by $R_{eff}(y) = \int dx B_z(x, y, 0)/B_z(0, 0, 0)$. Fig.3.8 shows that maximum deflection can be obtained at $y = -60$ mm.

Nonetheless, this is not the best possible configuration for our purpose because of the intrinsic unavoidable angular divergence. The situation is explained in fig.3.9 where the propagation of three 2 mrad beams of different energies ($50-100-300$ MeV)

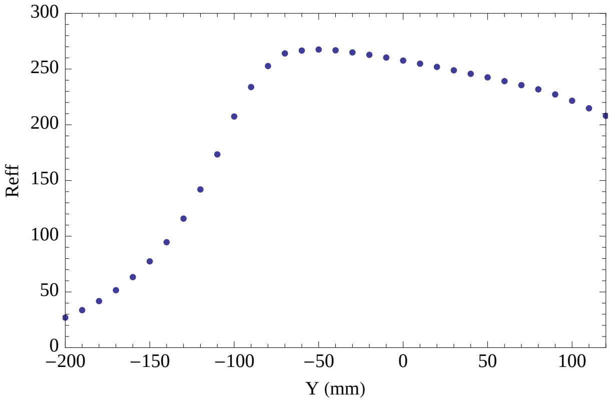

Figure 3.8. Effective radius as a function of the electrons entrance point.

is simulated. The simulation is based on the iterative Runge-Kutta methods for the approximation of solutions of ordinary differential equations. The equations of motion for an electron moving in the measured magnetic field are numerically solved using Mathematica.

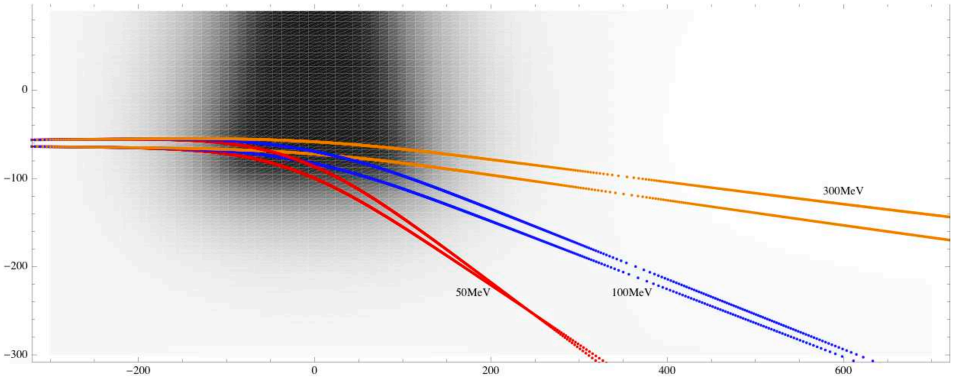

Figure 3.9. Propagation of three monoenergetic beams where the deflection is maximum: energy focalization not appreciable. In dark is the density plot of the magnetic field, with grayscale proportional to the intensity of the field.

If the electron beam is sent in correspondence of the fringe of the magnet, trajectories of the same energy up to a threshold with different initial directions will focus. The optimum position for the detector is given by the curve drown by the focii. Focii position, where focii exist, is independent of the initial divergence.

During the SITE experiment two detectors will be used: a low energy detector will collect electrons from 20 to 100 MeV while electrons with energy above 100 MeV and the laser beam itself will impact on the high detector. The position of the low energy detector is given by the position of the focii of the trajectories. The need to use two different arms for the detectors is dictated by the spatial constraints of the experimental hall.

Given the shape and intensity of the magnetic field, the magnet used for the first version of the spectrometer is not able to focus energies above 100 MeV. For this

reason the high detector is located as far as possible (perpendicular to the laser beam direction at a distance of 700 mm from the center of the magnet), so to increase the deflection for different energies. The situation is shown in fig.3.10 where also the detectors are drawn. The electron beam is shot at $y = -130$ mm, i.e.13 cm far away from the center of the pole axes.
As can be seen the detector total length is ~800 mm.

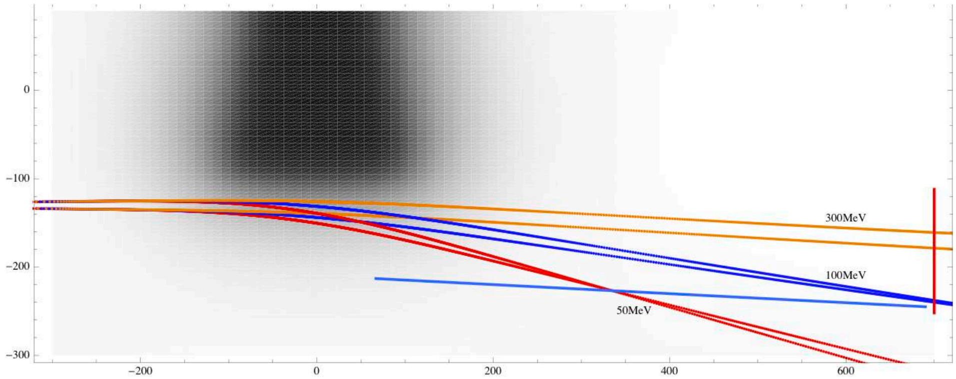

Figure 3.10. Propagation of three monoenergetic beams where energy focalization, for low energy particles, is appreciable. The red vertical line represents the high detector placed as far as possible, the blue one is the low energy detector placed on the focii.

3.1.2 The scintillating fibers

The requirement to detect simultaneously a huge number of particles spread over a large space lead us to an unconventional choice for the detector. In laser-plasma acceleration experiments in fact, as discussed in the first chapter, data are collected thanks to the use of lanex screens and CCD cameras. Obviously this choice is difficult to adopt for long detectors because of the intercalibrations, the synchronizations and the costs.

Our choice is to use plastic scintillating fibers. Fibers can be shaped on the required optimized position, are sensitive only to charged particles and can operate in vacuum. The spacial resolution is given by the dimension of the fiber and, even if is worse with respect to the lanex one, is not limiting the energy resolution in our case.

A scintillating material has the property to convert part of the energy deposited by a charged particle into light. A plastic scintillator consists of structural plastic in which small impurities were dissolved. An incident charged particle first interacts with the atoms of the scintillator exciting a primary fluorescent material which de-excites and emits photons in the ultra-violet. This light is absorbed within a mean free path of ~1 mm by a secondary fluorescent material also dissolved in the base plastic which emits in the visible part of the spectrum where the base plastic is fairly transparent.

A typical base plastic is polystyrene with a time constant for defluorescence of few ns. Typical *conversion efficiency*, i.e. the ratio between the emitted photon

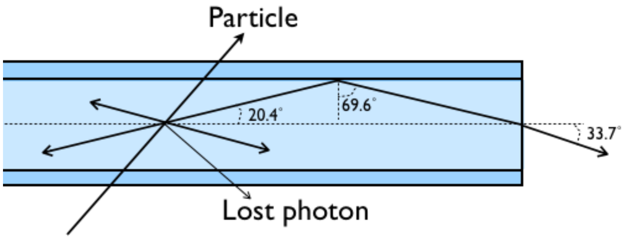

Figure 3.11. Transmission mechanism for single cladding scintillating fiber.

energy and the energy lost in the scintillating material, is ~1 photon per 100 eV of energy deposition. A one-mm-thick scintillator traversed by a minimum-ionizing particle will therefore yield $\sim$ 2000 photons (considering typical densities range from 1.03 to 1.20 g/cm^3). The resulting photoelectron signal will depend on the collection and transport efficiency of the optical package and the quantum efficiency of the photodetector.

As the light is emitted isotropically inside the material, there is a critical angle for the total internal reflection, θ_c. The critical angle is given by $\theta_c = arcos(n_{cl}/n_{co})$ so a fraction of the emitted photons are captured within the fiber and move towards one end. Considering the solid angle within which the total reflection occurs, we obtain the *trapping efficiency* $\Delta\Omega/4\pi = 0.5(1 - n_{cl}/n_{co})$.

We use Kuraray SCSF-81 round fibers with 1.00 ± 0.05 mm diameter. The internal part is called core and have refractive index $n_{co} = 1.59$. The core is of almost no oriented polystyrene (PS) chain and is optically isotropic and very transparent. The single cladding, 3% thickness of the whole diameter, is made of polymethymethacrylate (PMMA) with refractive index $n_{cl} = 1.49$. The trapping efficiency is 3.1%: this means that from the 2000 photons produced by a single electron only 60 photons are trapped. The emission peak is in the blue color at 437 nm with long attenuation length, $\lambda > 3.5$ m.

The whole detector, in fig.3.12 is composed by two arrays of fibers: we use 140 fibers for the high energy detector, placed perpendicular to the laser propagation direction, and 624 fibers for the low energy detector. The angle between the two is 87°, being the low detector almost parallel to the laser direction. The scintillating fibers are 50 cm long. They extend vertically and the ends are grouped in order to have an interface with the appropriate device able to collect data: photomultipliers or Charged Couple Device (CCD) cameras. In order to reduce the impact of electromagnetic noise during laser-plasma interactions, the fibers are bundled and fed to the PMT's, which are placed on a aluminum holding frame, at about 50 cm height from the beam-line.

However, as we expect very high electromagnetic pulse noise, it is important to have the possibility to measure the signal far away from the laser-plasma interaction region. For this reason, and because we expect also very high electron signal, we have realized 4 m clear fiber extensions that can be inserted between the scintillating

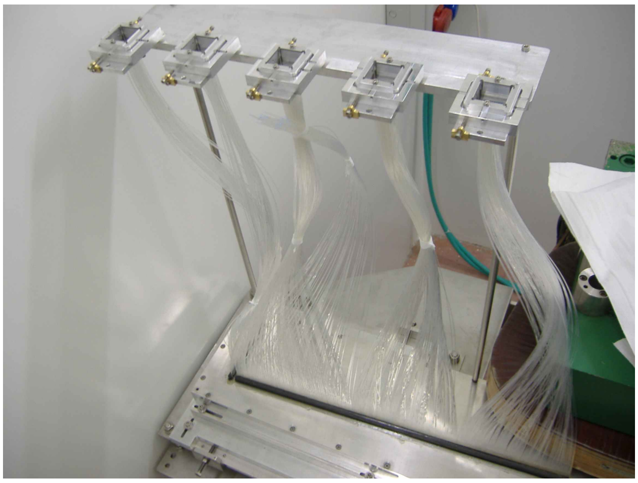

Figure 3.12. The scintillating fiber array used as detector.

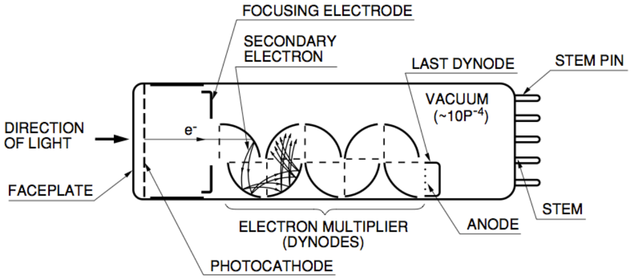

Figure 3.13. Construction of a photomultiplier tube.

fibers and the photodetector.

3.1.3 The photomultipliers

The light emitted from a scintillating fiber can be converted in electrical signal thanks to the use of photomultipliers (PMT). A typical PMT consists of a photoemissive cathode (photocathode) followed by electron multipliers (dynode stages) and an electron collector (anode), as indicated in fig.3.13.

The PMT we use are metal channel dynode structures combined with multianode readout HAMAMATSU H7546A. The main features are: the effective area of 18.1 mm×18.1 mm, over which is located a 8×8 multianode matrix with single anode size of 2 mm×2 mm; the high speed response; the low 2% typical cross-talk. In a multianode device, the output signal is read using different pins corresponding to the 64 independent multiple anodes. It is important to notice that the dynode12 output is separately connected to a terminal pin. The overall tube length can be kept short because the metal channel dynodes are very thin and assembled in close-proximity to each other. Fig.3.14 shows the electrode structure for metal channel dynodes and the associated electron trajectories.

The spectral response is in the range from 300 to 650 nm with a peak emission

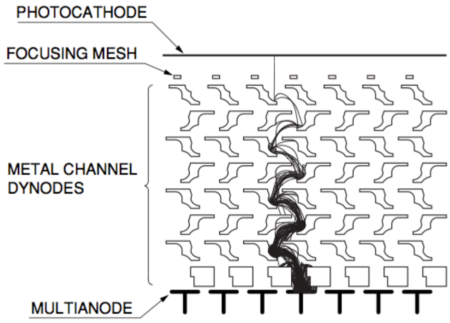

Figure 3.14. Electrode structure and electron trajectories.

at 420 nm. Maximum ratings for the supply voltage between anode and cathode is -1000 V, with nominal tension -800 V. The quantum efficiency is the number of photoelectrons emitted from the photocathode divided by the number of incident photons: for wavelength range between 300 and 450 nm is ∼20%. Fig.3.15 shows current amplification (gain) vs supply voltage.

In general the secondary emission ratio δ is a function of the interstage voltage of dynodes V, and is given by $\delta = a \cdot V^k$, where a is a constant and k is determined by the structure and material of the dynode (typical value range for k is 0.7-0.8). The photoelectron current I_k emitted from the photocathode strikes the first dynode where secondary electrons I_{dl} are released. The secondary emission ratio δ_1 at the first dynode is given by $\delta_1 = I_{dl}/I_k$. These electrons are multiplied in cascade from the n dynodes. At the last $n-th$ stage the secondary emission ratio δ_n is given by $\delta_n = I_{dn}/I_{d(n-1)}$. The anode current I_p will be proportional to collection efficiency α, the photoelectron current I_k and the secondary emission ratios of the different stages, in formula $I_p = I_k \cdot \alpha \cdot \delta_1 \cdot \delta_2 \cdots \delta_n$. The product $\mu = \alpha \cdot \delta_1 \cdot \delta_2 \cdots \delta_n$ is called *gain* (current amplification). It depends on the supply voltage as $\mu \sim (a \cdot V^k)^n \sim V^{kn}$. From this equation, it is clear that the gain μ is proportional to the kn exponential power of the supply voltage.

Since fig.3.15 is expressed in logarithmic scale for both the abscissa and ordinate, the slope of the straight line becomes kn and the current multiplication increases with the increasing supply voltage.

The time response is shown in fig.3.16: the full width at half maximum of the output pulse is ∼3 ns. This signal is read by the read-out system.

3.1.4 Detector design

As mentioned above the whole detector length is about 800 mm: 140 fibers for the high momentum particles and 624 fibers for the low momentum particle. To read each single fiber would require about 12 photomultipliers and ∼800 electronic channels: we have studied how to group the fibers in order to keep the best possible energy resolution but limiting the cost of the read-out system.

Because of the low deflection it is important to read each single fiber of the high

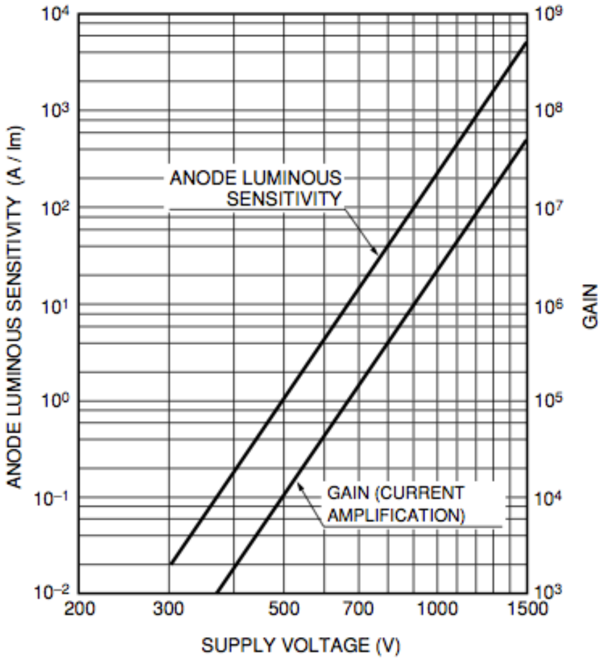

Figure 3.15. Gain vs. supply voltage.

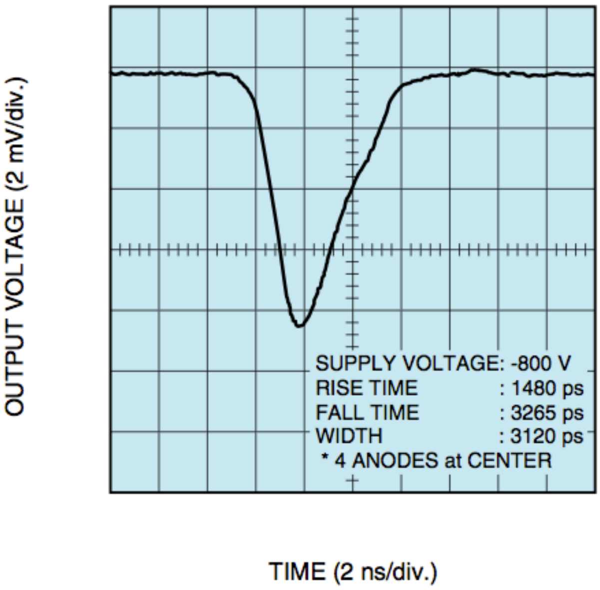

Figure 3.16. Time response.

energy detector placed perpendicular to the laser beam direction. The first 128 fibers are connected one by one to the pixels of two 64-channels photomultipliers (PMT 0 and PMT 1 in fig.3.17). The last 12 fibers of the high momentum detector are read in groups in three (first 4 pixels of the third photomultiplier, PMT 2). The trajectories impacting on the first part of the low momentum detector cross more than one fiber because of the strong impacting angle. We read three fibers with the same photomultiplier pixel, skipping one fiber between two groups, for a total number of 240 fibers (this completes the third photomultiplier). The remaining 384 fibers are still grouped in groups of three and fill the last two photomultipliers (PMT 3 and PMT 4).

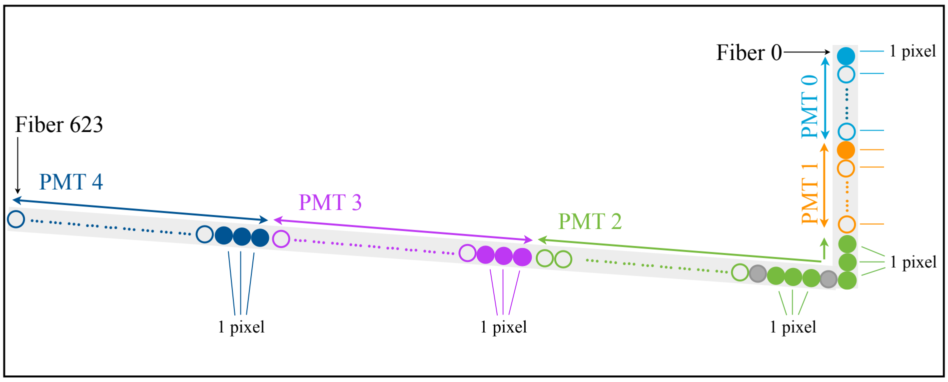

Figure 3.17. Schematic view of the fibers to PMT pixels arrangement.

Fig.3.17 shows a schematic view of the fibers-pixels arrangement. For each PMT is indicated how many fibers are grouped together to a single pixel.

To realize this configuration the fibers are glued onto aluminum drilled masks (two with single fiber holes, for the high momentum screen, and three with three-fibers holes for the low momentum screen, as shown in fig.3.18). Those mask are mounted on a two-dimensional adjustable frames, easy moveable by precision screws, in order to optimize the alignment between fibers and the pixel of the segmented PMT.

In total we have five 64-channel photomultipliers: in the next section the read-out system for the 320 electronic channel is described.

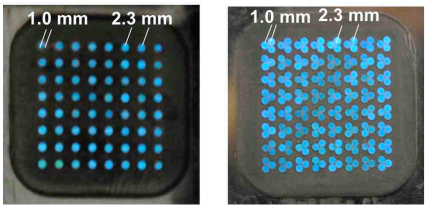

Figure 3.18. On left, single fiber holes mask used for the high detector. On right, three-fibers holes masks used for the low detector.

3.1.5 The read-out system

The anode output pins of each photomultiplier are connected to external chips thanks to a specifically realized connector (see fig.3.19) and a micro coaxial flat-cable Samtec.

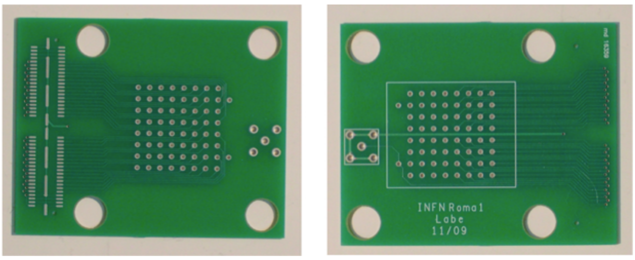

Figure 3.19. Connectors realized to connect the 64 anode output pins of each photomultiplier to external chips.

The connector is also provided with a lemo cable that outputs the dynode 12 signal for debugging purposes. We are using MAROC2 chips, Multi Anode ReadOut Chips version 2, developed al LAL-Orsay for the Atlas Luminometry [18].

The MAROC2 chip is a 64-channel input front end circuit to read out multi anodes photomultiplier outputs. It provides one shaped signal proportional to the input charge and 64 trigger outputs. Fig.3.20 gives a simplified schematic diagram of the whole chip.

Each channel is made of a variable gain preamplifier (to eventually compensate for the PMT gain dispersion). The amplifier current feeds then three possible paths:

- *fast channel path*: two possible fast shapers (unipolar and bipolar) are followed by a discriminator to deliver trigger outputs.

- *slow channel path*: one slow shaper (20 ns − 100 ns) with three switchable feedback capacitances to allow tuning peaking time of signal followed by two Track and Hold buffers. The first one is used to measure the baseline and the second one to store the signal charge. An operational transconductance amplifier (OTA) delivers the multiplexed charge.

The Maroc2 technology allows to multiplex up to 4096 channels: staring from the input signals of 64 different chips, the multiplexing realized after the two S&H generates a single signal with temporal delays such that allow to separate the signals at the end of the whole chain.

As appears in fig.3.21, the whole read-out system has three components:

- *controller*: connected via USB to the computer, it receives all the settings from the acquisition software and sends back the data after the acquisition. The controller needs a TTL trigger signal.

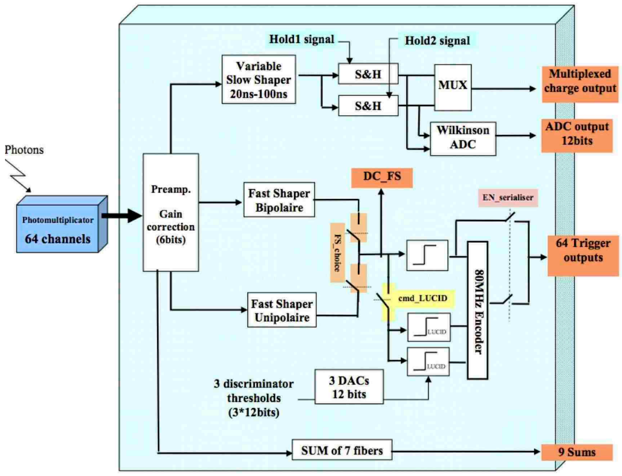

Figure 3.20. Block schematics of MAROC2 chips architecture.

- *backplane*: connected via flat cable to the controller. There are 8 numbered slots for the MAROC2 chips.
- MAROC2 *chips*: an arbitrary number of chips can be used, paying attention to fill always the first slot.

Both controller and backplane are powered at +3.9 V, with a total current depending on the number of MAROC2 chips used (for five chips ∼2 A).

The choice of the front end card was studied in collaboration with INFN BA, GE and ISS-Roma1.

When is operating the full electronic chain for each electronic channel (corresponding to PMT's pixel) the DAQ (see next section for details) register a number proportional to the impacting charge on each fiber of the detector. This information is directly mapped into a position spectrum and is the starting point for the energy spectrum reconstruction.

3.1.6 Data acquisition software

The data acquisition is performed with a C++ application using the ROOT framework. A binary file (.bin) recording the ADC counts for each electronic channel of the Maroc2 chips in use is stored. The main parameters controllable via a config.txt file are:

- the number of events to collect or the time of a single run (in s): the run ends when one of the two is recorded;
- the software delay time between signal and trigger: it is a number in the range 0−255 s that allow to delay the integration window with respect the PMT signal response in order to integrate the signal on the minimum (negative signal response) and not on the tails;

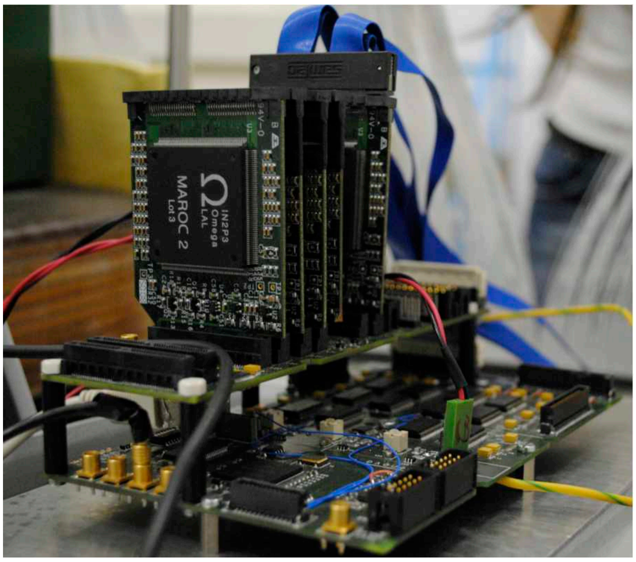

Figure 3.21. The read-out system components: MAROC2 chips, backplane and controller board.

- the electronic gain: a number from 2 (1/8×) to 64 (4×) related to the pre-amplification of the signal at the entrance of the Maroc2 chip. This scans a range of 32. When operating with high signals this gain parameter allows to reduce the signal to convert in ADC counts, avoiding saturation effects.

For each electronic channel the acquisition tool produces an ADC counts histogram. When the light source is switched off (LED off) we observe a pedestal value: typical values in the range of $1550 - 1650$ counts. Fig.3.22 shows the signal observed in a single channel switching off (left) and on (right) the LED. In general, the observed pedestal (here is shown a pedestal of ∼1600 counts) slightly depends on the channel, on the applied tension and on the number of chips in use fluctuating in the range $1550 - 1650$. It represents the low limit value for the ADC counts (see fig.3.22 on left).

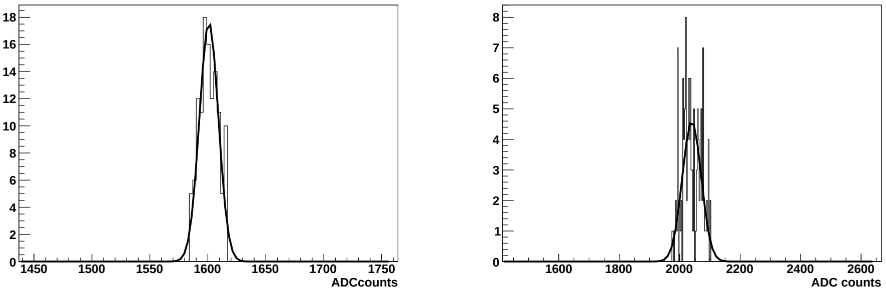

Figure 3.22. ADC counts histogram for a single PMT channel when the LED is switched off (left) and on (right).

We have observed that the dynamic range of the electronics is about ∼800 counts, with a saturation limit around ∼2400 counts: keeping increasing the external signal, the ADC counts do not change. When the light source is switched on (LED on) we observe a distribution like the one shown on right in fig.3.22.

The data analysis is done in single mode – analyzing event by event when operating in normal LPA conditions, because of the fluctuations between different shots – or in multi event mode – taking the average of the events when we operate with stable and reproducible sources (during calibration tests).

For a single event, for each channel, the ADC counts histogram is fitted using a Gaussian distribution. Mapping the electronic channels into the fiber numbers, a plot of the mean ADC counts versus fiber number is produced. The map used for the mapping is shown in fig.3.23 and depends on the particular pattern chosen for connect the fibers to the PMT pixels. We use zig-zag pattern in order to minimize the optical cross-talk between near fibers.

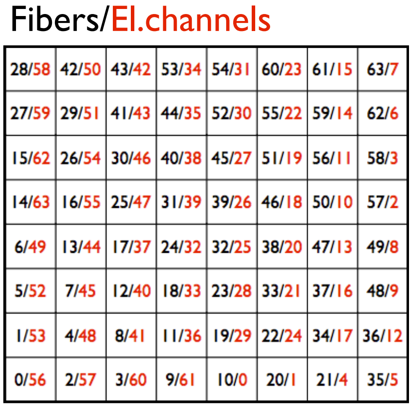

Fibers/El.channels

28/58	42/50	43/42	53/34	54/31	60/23	61/15	63/7
27/59	29/51	41/43	44/35	52/30	55/22	59/14	62/6
15/62	26/54	30/46	40/38	45/27	51/19	56/11	58/3
14/63	16/55	25/47	31/39	39/26	46/18	50/10	57/2
6/49	13/44	17/37	24/32	32/25	38/20	47/13	49/8
5/52	7/45	12/40	18/33	23/28	33/21	37/16	48/9
1/53	4/48	8/41	11/36	19/29	22/24	34/17	36/12
0/56	2/57	3/60	9/61	10/0	20/1	21/4	35/5

Figure 3.23. In black is the pattern chosen for the fibers, in red are written the corresponding electronic channels.

The analysis applied to a pedestal run gives the plot shown in fig.3.24. The pedestal values vary slightly from channel to channel.

Illuminating only one of the 64 fibers we obtain the plot in fig.3.24 where is clearly visible the signal on a single fiber.

3.1.7 The CCD-based data acquisition system

The electron spectrometer is also provided by a purely optical read-out system. It is based on CCD cameras. It completely substitutes the devices used after the fibers (PMT+MAROC+electronics). The light emitted by the scintillating fibers is directly detected and analyzed by CCD cameras (see fig.3.25). As discussed in the historical overview, CCD cameras are widely used in this field because, being properly shielded, they don't suffer the high electromagnetic noise.

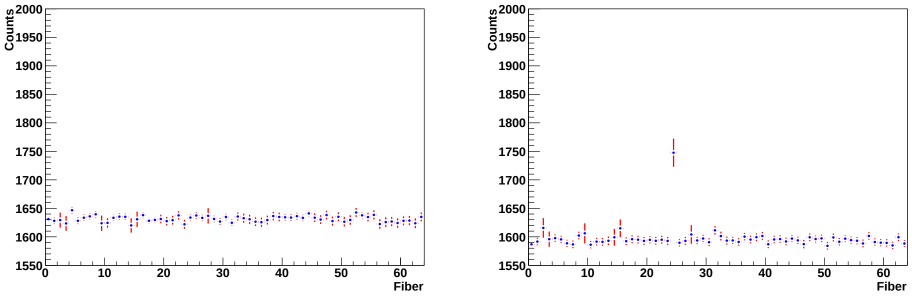

Figure 3.24. Left: ADC counts versus fiber number when the light source is switched off: pedestal values. Right: ADC counts versus fiber number when the light source is illuminating a single fiber.

Figure 3.25. The CCD camera based read-out system replaces all the devices used after the fibers, directly detecting the light emitted by the scintillating fibers .

We are using Basler A600f cameras with square pixels of size 9.9 μm, for a total number of 656(H)×491(V) pixels. The cameras are fixed on two-dimensional adjustable frames, easy moveable by precision screws, in order to optimize the alignment and the focalization.
The important performance specifications are: the nominal power requirement is +12 VDC; the cameras need an external trigger signal for synchronization; the gain, the brightness and the exposure time are programmable via software.

When is operating the optical read-out system, the CCD images are analyzed identifying the pixels corresponding to the signal of a single fiber (details following). We obtain a position spectrum that, as in the case of the electronic read-out system, is the starting point for the energy spectrum reconstruction.

3.2 Data analysis: the electrons energy spectra reconstruction

In the following section the general scheme used for the data analysis is described and it is independent on the particular data-acquisition system used during the acquisition.

Our final aim is to evaluate the energy spectrum of the accelerated electrons, i.e. the number of particles with energies in a given range.

The starting point is the measured position spectrum where the electrons arriving in a given space range are counted.

To unfold the distribution from a position measurement to an energy distribution we use the Bayesian approach. It makes use of the concept of causes and effects [19].

In our case, a general cause C_i is interpreted as the presence of electrons with momentum p_i, while the effect E_j is interpreted as the observed charge in the j-th fiber. The number of causes n_C is thus the chosen number of bins for the momentum range under study, and the number of effects n_E is the number of observed charges (number of the electronic channels in use).

In the unfolding procedure there are two important steps: first − generate the *smearing matrix*: given the initial momentum of the particle calculate distribution of the final position on the detector; second − use the smearing matrix *to infer* the probability that a hypothesis may be true.

3.2.1 The smearing matrix: detector response characterization

In general, if we observe $n(E)$ events with effect E, the expected number of events assignable to each of the causes is

$$n(C_i) = n(E) \cdot P(C_i|E). \tag{3.1}$$

where $P(C_i|E)$ is the conditional probability of the i-th cause to be true if observed the effect E. Let us assume we know the initial *a priori* probability of the causes $P_0(C_i)$ and the conditional probability $P(E_j|C_i)$ of the i-th cause to produce the effect j. As the outcome of a measurement we have several possible effects E_j ($j = 1, 2, \ldots, n_E$) for a given cause C_i. For each of them the Bayes formula

$$P(C_i|E_j) = \frac{P(E_j|C_i) \cdot P_0(C_i)}{\sum_{l=1}^{n_C} P(E_j|C_l) \cdot P_0(C_l)} \tag{3.2}$$

holds, and $P(C_i|E_j)$ can be evaluated. We observe that:

- $P_0(C_i)$ is the *a priori* probability to generate a particle with energy i. This probability is updated with multiple iterations of the Bayesian theorem.
- $\sum_{i=1}^{n_C} P(C_i|E_j) = 1$: this normalization condition, mathematically trivial, says that each effect must come from one or more of the causes under examination.
- The final distribution depends on the conditional probability $P(E_j|C_l)$, called *smearing matrix* S. This can be estimated with Monte Carlo simulations.

In our case to estimate the smearing matrix $P(E_j|C_i)$ means to simulate the probability of the momentum i to release charge in channel j. We simulate a flat distribution in the expected range of operation $0.02 - 1.62$ GeV.

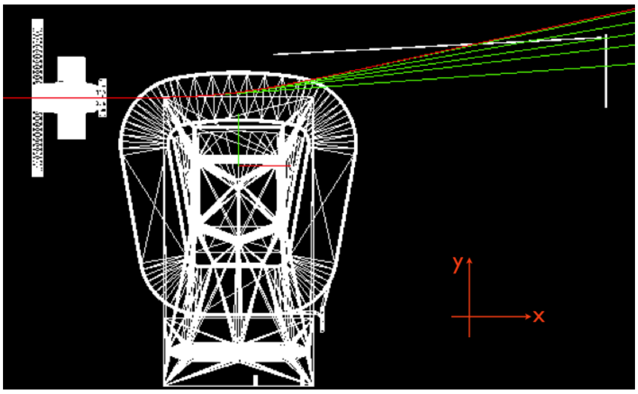

Figure 3.26. Geant4 simulation to calculate the smearing matrix.

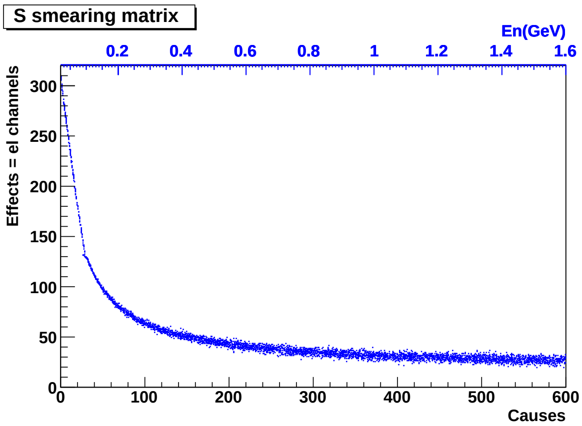

Figure 3.27. Smearing matrix.

We calculate the smearing matrix using a Geant4 based simulation taking into account the experimental set-up and the measured magnetic field (details on the simulation are given in the following section). The Smearing matrix can be visualized as a 2D histogram where the $x-$axis represents the causes and the $y-$axis the effects. In our case the causes are the energies, simulated in a realistic range from 0.02 to

1.62 GeV considering a gaussian angular divergence of σ=2 mrad, binned in 600 bins. The effects are the signals of the electronic channels, 320 bins for 320 channels. For a fixed energy−channel pair of the plot shown in fig.3.27, the box area is proportional to the probability $P(E_j|C_i)$ of the energy i to release signal in channel j.

As it can be seen, for low energies (<100 MeV corresponding to the low momentum detector) the S matrix is very narrow (few channels for a given energy) as expected because of the focusing property. For high energy particles the shape on the S matrix becomes broader.

3.2.2 The Bayesian inference

Here we discuss the mathematical details of the unfolding, giving at the end of the section the loop to follow for an iterative procedure.

After N_{obs} experimental observations we obtain a distribution of frequencies $n(E) = n(E_1), n(E_2), \ldots, n(E_{n_E})$. The expected number of events to be assigned to each of the causes can be calculated applying eq.3.1 to each of the effects. We have:

$$n(C_i) = \sum_{j=1}^{n_E} n(E_j) \cdot P(C_i|E_j). \tag{3.3}$$

From this unfolded events we can estimate the final probabilities of the causes:

$$P(C_i) = P(C_i|n(E)) = \frac{n(C_i)}{\sum_{i=1}^{n_C} n(C_i)} \tag{3.4}$$

Here we observe that staring from the assumed know initial probability of the causes $P_0(C_i)$, we obtain a new definition for the same quantity, as given by eq.3.4. This suggests to proceed iteratively. Fixing the number of iterations, the unfolding can be performed through the following steps:

1. choose the initial distribution of $P_0(C)$ from the best a priori knowledge of the process under study, and hence the initial expected number of events $n_0(C_i)$; when $P_0(C)$ is considered to be a uniform distribution (in case of complete ignorance) we have $P_0(C_i) = 1/n_C$;

2. calculate $n(C)$ and $P(C)$ using eq.3.3 and eq.3.4 respectively;

3. replace $P_0(C)$ by $P(C)$ in eq.3.2 and start again, stopping when the chosen number of iteration is achieved.

The main point of the iterative procedure is: once we have evaluated the number of events to be assigned to each of the causes, or better the vector $n(C)$, through the Bayesian theorem we can use this information to update the *a priori* probability in the Bayesian formula and proceed to evaluate $n(C)$ again.

The final distribution we are interested in is the vector $n(C)$, containing the number of events to be assigned to each of the causes.

The unfolding studies have been done both with single bayesian loop, and considering a higher number of iterations in order to find a stable regime in the process. As we will show in the next section after 10 iterations the final unfolded distribution does not change significantly even if increasing the number of unfolding loops.

3.3 Energy resolution

The expected energy resolution is given by the combination of two components: the spatial resolution of the detector (1 mm of diameter) and the initial angular divergence of the beam. Being the low momentum detector designed to focus trajectories with the same energies, we expect a much better resolution with respect to the high momentum detector. Here we discuss the way to estimate the energy resolution and quantify what is expected.

For a given momentum p_i we simulate a beam with a gaussian energy distribution centered in p_i and a 1% spread. The angular divergence is assumed to be gaussian distributed. The momentum range is $0.02 - 1.62$ GeV, binned in 600 bins. The true momentum distribution defines the vector $n(C)$. The ADC counts of a single cannel $n(E_j)$ are evaluated as:

$$n(E_j) = \sum_i n(C_i) P(E_j|C_i) \tag{3.5}$$

where the conditional probability $P(E_j|C_i)$ is given through the smearing matrix. The vector $n_(E)$ defines the smeared distribution as the number of ADC counts versus the position on the detector. At this point the unfolding procedure described in sec.3.2.2 is applied and we obtain the unfolded momentum distribution.

The energy resolution is defined by

$$res = \sqrt{|(\frac{\sigma_{unf}}{\mu_{unf}})^2 - (\frac{\sigma_{true}}{\mu_{true}})^2|} \tag{3.6}$$

where for both the true and the unfolded distribution a gaussian fit is used to define the mean and the sigma values.

From the red boxes in fig.3.28 we can see that the low momentum detector is characterized by a resolution less then 1%. Up to 300 MeV we have resolutions less then 5%: the worsening with increasing momentum is clear. Performances between low and high detector will be different mainly because of the angular effect for the high energies. As suggested in sec.3.2.2 we can proceed iteratively.

In fig.3.28 the green triangles show the expected energy resolution considering 10 unfolding iterations. We have a significant improvement for the high momentum detector (up to 800 MeV we have resolutions less then 5%).

Fig.3.29 shows the reconstruction of beam with a gaussian energy distribution centered in $p = 100$ MeV and a 1% spread. The reconstructed energy spectrum is independent on the number of Bayesian iterations used as can be seen from the red (one iteration) and orange (ten iterations) shapes.

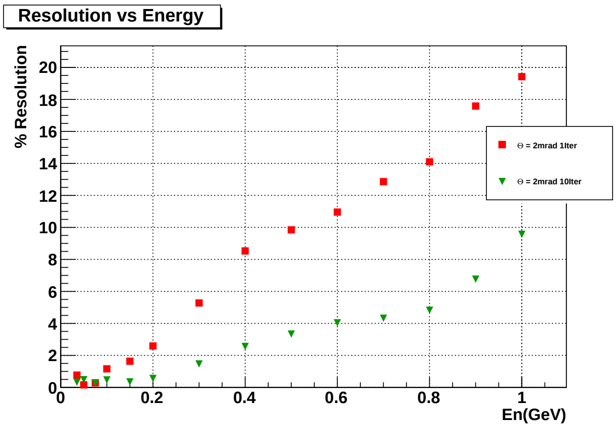

Figure 3.28. Expected energy resolution considering one (red boxes) and ten (green triangles) Bayesian iterations.

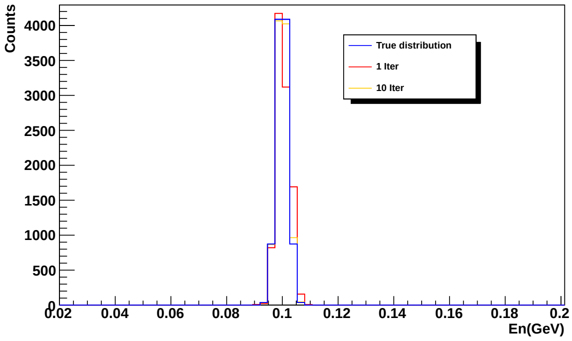

Figure 3.29. Energy reconstruction for a beam with a gaussian energy distribution centered in p=100MeV and a 1% spread shown in blue. In red is shown the result for a single Bayesian iteration, in orange the unfolding obtained with 10 iterations.

For comparison, fig.3.30 shows the same analysis done with beam with a gaussian energy distribution centered in $p = 1$ GeV and a 1% spread. After one unfolding iteration we obtain a broad energy spectrum that gives the correct information about the mean value of the energy distribution. After ten Bayesian iterations the unfolded distribution narrows, giving as result a better energy resolution. The number of iterations can't be increased at will because the procedure may accentuate small counts excesses leading to false peaks.

3.4 Geant4 based simulation

In the previous chapter we have characterized the expected accelerated electron beam in the optimized laser-plasma interaction conditions trough a 3D PIC simulation. The main characteristics are summarized in fig.2.7 and fig.2.8 showing the energy spectrum and the expected angular dispersion distribution, respectively. Now, in

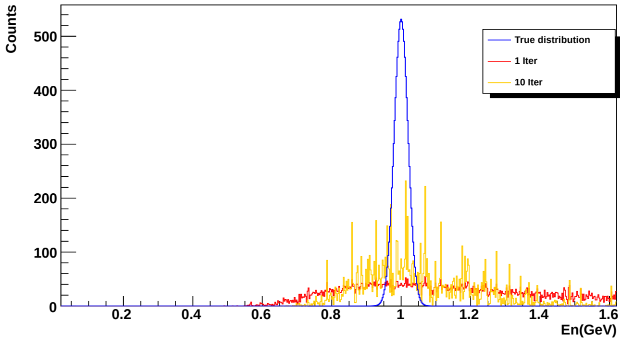

Figure 3.30. Energy reconstruction for a beam with a gaussian energy distribution centered in $p = 1$ GeV and a 1% spread shown in blue. The broad red distribution shows the unfolding result after one iteration, in orange is shown the result for 10 iterations.

this section, our attention is focused on a better understanding of the detector response and of the possible noise caused by the particles at high divergence. Here we will discuss the results of a complete Geant4 based simulation taking as input the particles produced in the PIC simulation.

We use the Geant4 platform to simulate the passage of particles through matter. Geant4 includes facilities for handling geometry, tracking and detector response.

The basic concept in the construction of the detector is the volume. The detector is made of volumes, each volume being contained in a larger volume. The largest volume is called the world volume. Each volume is defined by its geometrical shape, dimensions, position and material. When working with a particularly complex geometry, it can be defined using the Computer-Aided Design (CAD) of the complete layout of the experiment. The CAD is translated in a .gdml file containing the coordinates of every single device of the electron spectrometer. The flanges that connects the vacuum interaction chamber to the beam pipe, the dipole and its coil, the beam pipe and the array of scintillating fibers are all defined independently so that the user can switch on or off their presence in the simulation (gaining elaboration time). Also the material of the volumes is specified through the .gdml file. In order to define materials we need to define first elements giving the atomic number, number of nucleons and atomic mass. The material is defined its macroscopic properties: density, state, temperature, pressure. Also the vacuum is treated as a material.

The magnetic field is interpolated from the experimental measurements of the magnetic field. The geometry and the materials of the detector are defined in a class called DetectorConstruction.

Geant4 can give us information about the status of the simulation at three levels: the run, the event and the track. A run is a simulation that includes a certain number of events. An event is an interaction between one beam particle and the detector (including all interactions caused by the products of the first reaction). In each event, a number of (primary and secondary) particles are present. These are called tracks in the simulation.

Tracking is simulating the passage of particles through matter. This involves considering possible interactions. For electrons we consider multiple scattering, electron ionization, electron bremsstrahlung, synchrotron radiation; while for gammas we have Compton scattering, photo-electric effect and conversion to $e^+ \ e^-$ pairs. This processes are defined through the PhysicsList class and can be activated or not in a simple way through a configuration file.

Detector response is recording when particles pass through the volume of a detector, and approximating how a real detector would respond. We store information about the event in an output .txt file in order to see what interactions each particle has initiated, how much energy was lost in them, which is the parent particle of the track, etc. How detailed this information is chosen by the user and set by the verbosities of the run in the configuration file.

The simulation is also provided with a visualization manager. The detector has a default top view which can be rotated by the user. The tracks are drawn at the end of event, and erased at the end of run. Optionally one can choose to draw all particles, only the charged one, or none.

The primary (source) particles are the one simulated via 3D PIC code and discussed in fig.2.7 and fig.2.8. These electrons are characterized in momentum immediately after the gas jet, so they have to propagate in vacuum at least for 1 m before reaching the detector. Using a Geant4 simulation we control the propagation of all the tracks and their interaction with the detector.

What we expect is that the initial electron beam arrives at the detector without significant distortions: if this is the case we are sure to observe on the detector the beam out-coming from the plasma, without the possible noise caused by the particles at high divergence. This is the first study discussed in the next section about electron signal.

The second aspect we are interested in is the energy reconstruction. The output file, for a fixed track, contains the position, energy, location, type of iteration at each simulation step. Having access both at the position and at the energy distribution of the electrons on the detector we perform a comparison between the observed energies on the detector (we call this true distribution) and the unfolded energy spectrum obtained through the bayesian procedure taking as input the electrons position distribution on the detector.

Having access to all the tracks we estimate also the expected photon signal given by the secondary photons produced in electrons interaction, on order to evaluate their possible contribution to the production of optical photons.

3.4.1 Expected electron signal

The electron produced in optimized conditions of laser-plasma interaction have the energy spectrum shown in fig.2.7. Using a Geant4 simulation we let this bunch to propagate in vacuum, until to reach the electron detector.

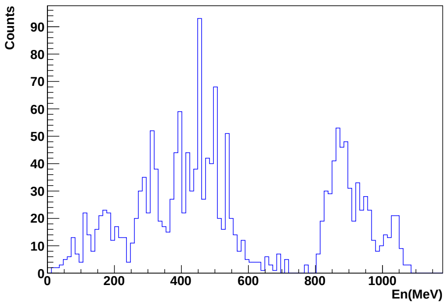

Figure 3.31. Energy of the electrons observed on the scintillating fibers.

Fig.3.31 shows the output of the simulation in terms of electrons energy as observed on the scintillating fibers. There are no significant distortions in shape with respect to the 3D PIC simulation discussed in fig.2.7. A plot of the electron signal on the detector is shown in fig.3.32. The fiber are mapped into electronic channels so to have a view of what expected during the experimental data taking. We remember that channel 0 corresponds to the fiber 0 of fig.3.17, and the channel number increase with decreasing energy.

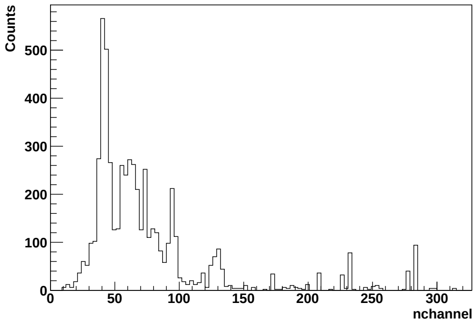

Figure 3.32. Electron signal distribution on the electronic channels.

This position measurement has to be unfolded in order to obtain the reconstructed energy spectrum. Fig.3.33 shows the superposition of the true observed energy distribution (as out-coming from the Geant4 simulation) for both one (left plot) and ten (right plot) bayesian iterations: the reconstructed spectrum is close to the true one and the two components can be clearly identified; as expected, the reconstruction at high energy is broader than the true distribution. The width of the two structures is better estimated increasing the number of iterations.

Since the detector is not optimized for this final configuration, it is of interest to consider the response of the detector to lower energies. Lowering the energy, the electron signal is expected at higher channels, as demonstrated in fig.3.34.

Fig.3.35 shows in blue the true distribution, rescaled by a factor 4 with respect

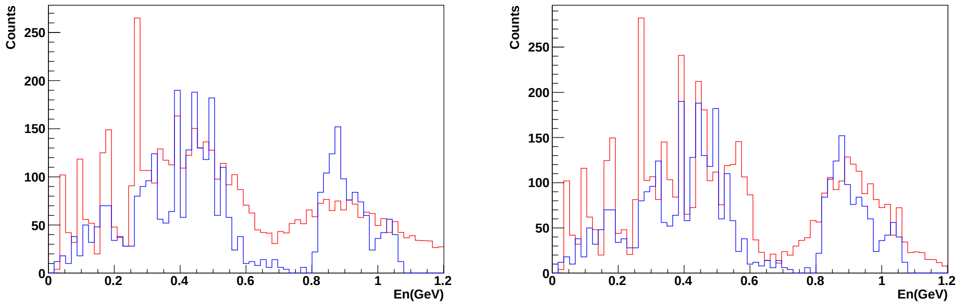

Figure 3.33. True (in blue) and unfolded (in red) full energy distribution, considering one and 10 bayesian iterations.

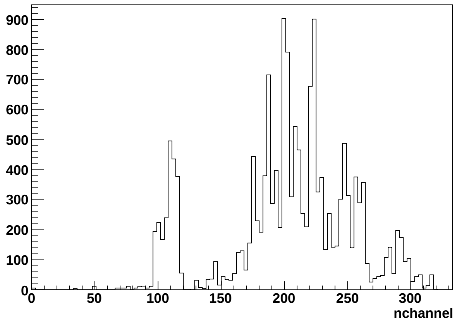

Figure 3.34. Electron signal distribution on the electronic channels when rescaling the energy of the bunch.

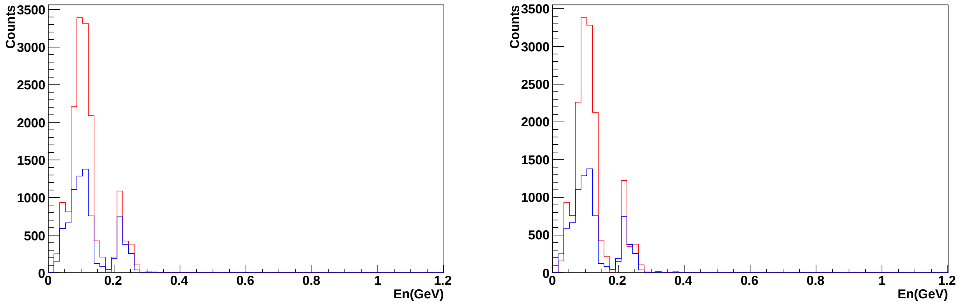

Figure 3.35. True and unfolded rescaled energy distribution, considering one and 10 bayesian iterations.

to the 3D PIC simulated expected distributions discussed in sec.2.1.3. In red is shown the unfolded distribution considering one (plot on the left) and ten (plot on the right) Bayesian iterations. Together with the very good reconstruction, the most significant aspect is the stability in the reconstruction even if considering a higher number of iterations.

3.4.2 Expected photon signal

One problem that we have studied is the possible generation of signal from the photons produced by electron interactions, in particular the synchrotron radiation.

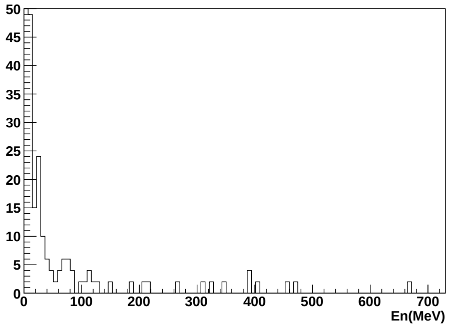

Figure 3.36. Energy distribution of the photons produced by electrons interactions.

Simulating the propagation of the full energy bunch discussed in sec.2.1.3 we select and study the produced photons. Fig.3.36 is the energy distribution of the photons that impact on the detector. The distribution presents long tails up to hundreds of MeV, but the light yield in the scintillating fibers is small.

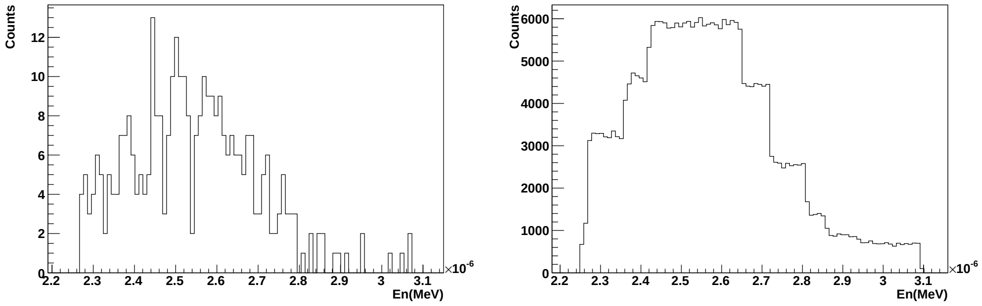

Figure 3.37. Optical photons produced by photons, on left, and electrons, on right.

The number optical photon produced by the gammas of fig.3.36 in a single fiber is negligible with respect to the number of optical photon produced by same amount of electrons. The two situations are shown in fig.3.37: the result of the simulation shows a factor 10^3 between the two signals, given by the integral of the two distributions.

From this study we can conclude that the electron spectrometer does not suffer the light source and the final electron signal is not affected by the electron secondary emissions. Thanks to the analysis tool we are able to reconstruct energies in the hundred of MeV range, while an upgrade of the spectrometer is required to a better analysis at higher energies.

Chapter 4

The performance of the electron spectrometer

To characterize the detector described in the previous chapter we have studied the performances using a prototype. An array of 64 scintillating fibers is connected to a photomultiplier and the out-coming signal is read by the electronic system. We have studied how to limit and solve the problems that may arise during the data acquisition and the results are discussed in the first section of this chapter. The second section is centered on the calibrations required in order to convert the observed ADC counts in electric charge, once the magnetic field map is validated.

4.1 Laboratory test of the whole chain with a first prototype

We have designed a prototype with the same components of the final detector discussed in sec.3.1. It is an array of 64 scintillating fibers, connected one by one to the 64 pixels of a PMT. The signal produced is read by a Maroc2 chip and converted in ADC counts by the electronic read-out system. Here below we discuss the whole signal propagation and the possible problems that may occur. These are mainly related to the dynamic range of all the components (saturation effects), the possible misalignment between the fibers and the PMT (cross-talk effects) and the synchronization between signals (timing).

4.1.1 Electronics parameters

Here we are interested in the effects of electronic gain and timing delay parameters on the observed signal.

For calibration tests we operate with a light-emitting diode (LED). The electronic trigger signal is a TTL signal with length in the range $80 - 250$ ns. The electronics is powered at 3.7 V and the forward current depends on the number of Maroc2 chips in use ($\sim$ 1 A for one chip inserted). The LED is operating at 1 Hz with 500 ns duration length. When the nominal tension ($\sim$800 V) is applied to the PMT we obtain the signals shown in fig.4.1: the PMT signal response is in blue and the

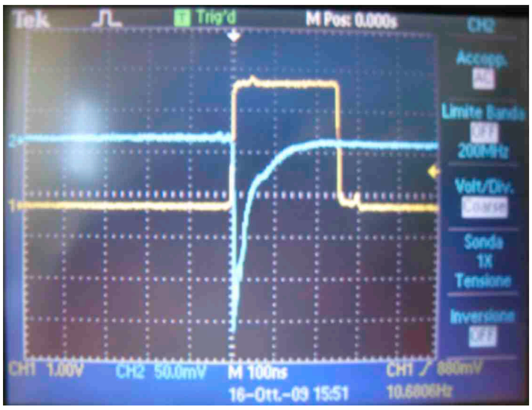

Figure 4.1. In blue is shown the PMT signal response when the fibers are illuminated with a LED. The yellow signal is the TTL trigger sent to the read-out electronic system.

trigger sent to the read-out system is in yellow.

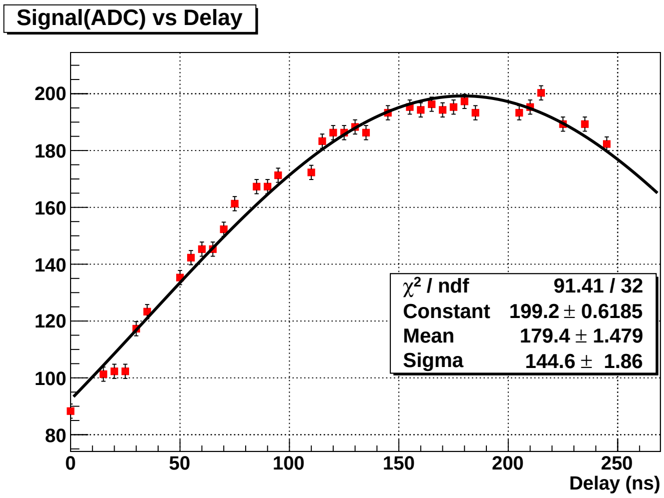

Figure 4.2. ADC counts versus delay.

Via software it is possible to delay the trigger with respect the signal in the range of $(0-250)$ ns, in order to integrate the minimum of the PMT response (which is negative). Scanning this value we obtain the behavior shown in fig.4.2, which is as expected because the integrating window moves over the PMT signal passing through a maximum when is in time, and integrating less signal when is on the tails. During this study the PMT is powered at 300 V, the input signal is a LED square wave of 200 ns, 4 V amplitude, and the hardware delay observed at the oscilloscope is $\sim$60 ns (this depends on the cable length in use).
Another parameter that we may vary via software is the electronic gain. This is a coefficient used by the preamplifier to multiply the signal immediately before the shaper. Fig.4.3 shows the linearity between the gain factor (possible range from 2 to

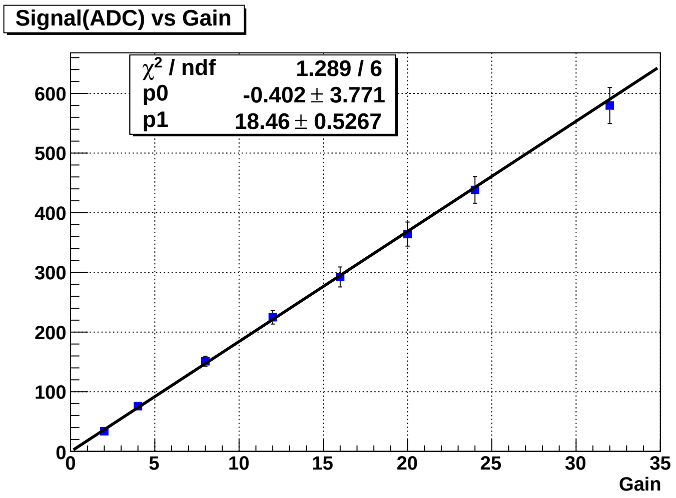

Figure 4.3. ADC counts versus gain.

32) and the ADC counts observed for a single channel. Again the PMT is at 300 V. Normally we operate with the default gain value, set to 2.

4.1.2 PMT high voltage study

In normal LPA conditions we expect to have high intensity input signals because of the expected $10^1$0 accelerated electrons. In this section we study when and how PMT saturation effects arise. In general, the saturation of a photodetector is defined as the phenomenon in which the amount of output signal is no longer proportional to the incident light intensity. The saturation may occur if the emission of photoelectrons is too high, leading to a current on the photocathode that lowers the tension between the photocathode and the first dynode; or if the currents are so high to reduce electric fields in the last steps of the photo-multiplication process.

To understand the PMT response to increasing signal we operate with a LED source and keep increasing the tension from 1.5 to 8 V. All the other parameters are fixed, in particular the PMT tension is 600 V, the electronic gain is 2. As already mentioned the dynamic range of the acquisition is 800 counts.

What we observe in fig.4.4 is the saturation of the PMT, in fact even if the amplitude of the light signal is increasing the observed ADC counts remain constant at a value inferior with respect to the saturation of the electronics. The saturation occurs when the LED tension is 4 V.

A second aspect that needs to be investigated is the calibration in applied high voltage. Because of the extremely high expected signals and the limited dynamical range of the electronics, it may be necessary to lower the PMT HV during the normal condition of the laser-plasma acceleration experiment and we need to know the PMT gain on a large HV range.

Looking at the fig.3.15 we observe that at the nominal tension of 800 V corre-

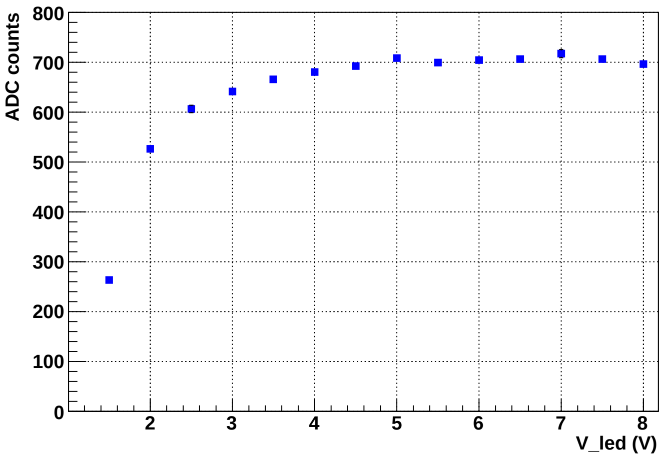

Figure 4.4. ADC counts as a function of the LED tension.

sponds a gain (current amplification) of 4×10^5: the gain increases up to 2×10^6 at the maximum allowed tension of 1000 V.

Being the electronic range of ∼800 units it will be sufficient to vary the PMT tension in a 300 V range: in general there will be a minimum threshold tension at which the signal will be significantly different from the pedestal value and at a tension 300 V higher we will observe the electronic saturation.

We use a LED source to directly illuminate the sensitive surface of the PMT. We expect that the threshold and the saturation tension are slightly different between different channels mainly because of the fact that the light signal is hard to be uniform (and to be quantified) on each channel. The LED amplitude is fixed, as well as the electronic gain g=2, and the only parameter that is scanned is the PMT tension.

For a selected PMT channel, fig.4.5 shows the ADC counts as a function of the applied HV tension in a 400 V region where is clear the threshold and the saturation tension.

Fig.4.6 shows data (red boxes) and fit result (black curve) for a single channel when the tension is scanned from 500 to 900 V. In ordinate we have the PMT signal normalized to the value obtained at 700 V. The fit function is:

$$f(x) = \frac{1 + P_0}{e^{-xP_1} + P_0} \tag{4.1}$$

which considers both the exponential and the saturation behavior being:

$$f(x = 0) = 1, \qquad f(x \to -\infty) = 0, \qquad f(x \to +\infty) = \frac{1 + P_0}{P_0}. \tag{4.2}$$

The parameter P_0 considers both the inflection point and the asymptotic behavior, while P_1 refers to the slope of the exponential.

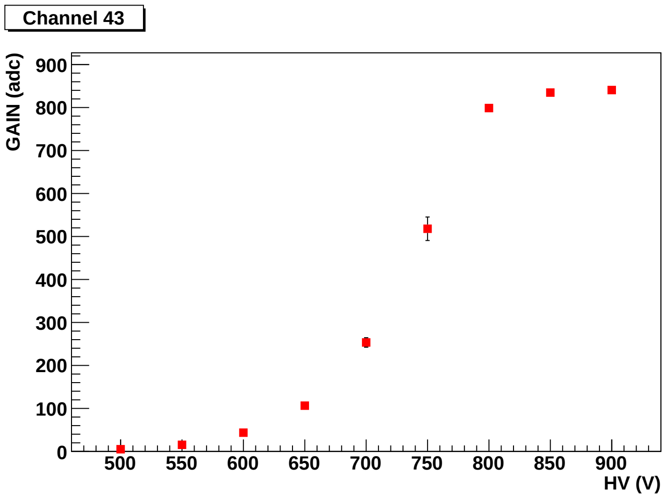

Figure 4.5. Single channel: ADC counts as a function of the HV tension.

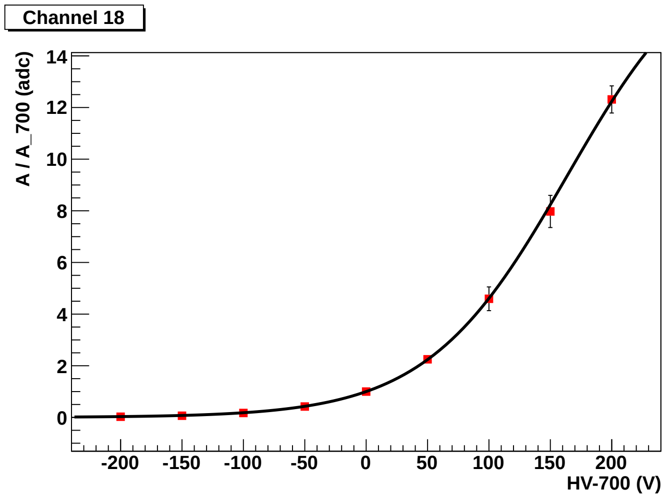

Figure 4.6. Single channel normalized ADC counts as a function of the HV tension minus 700 V. Data are in red boxes, fit result is in black curve.

This analysis has been done for all the channels with significant data – problems with a uniform light distribution over all the sensitive PMT surface reduce the number of analyzed channels.

Fig.4.7 and fig.4.9 show the histograms for the fitted parameters. The considered data refer to 39 of 64 channels, considering only good fits with $\chi^2 < 8$. The slope of the exponential, given by the parameter P_1, can be tested to be independent on the P_0 parameter using as fit function:

$$f(x) = \frac{P_0}{e^{-(x-P_2)P_1} + 1} \tag{4.3}$$

where P_0 considers the asymptotic behavior, P_1 the exponential slope and P_2 the inflection point.

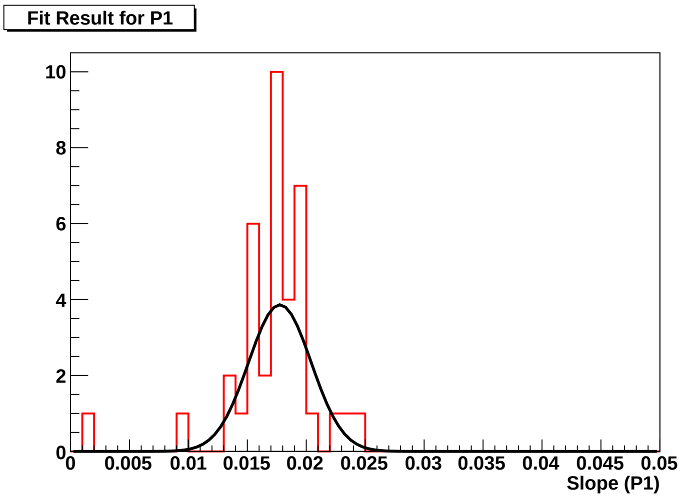

Figure 4.7. Histogram and fit for the P_1 parameter considering 39 channels of 64.

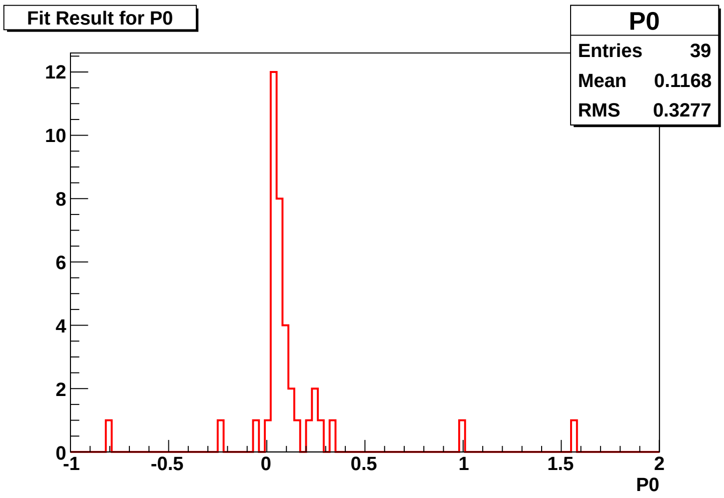

Figure 4.8. Histogram for the P_0 parameter considering 39 channels of 64.

Fig.4.9 shows this fit result for the same channel studied in fig.4.6 with the normalized function. As it can be seen the value of the obtained parameter P_1 is in agreement in both the analysis.

The different channel response (gain) to the applied tension out-coming from the result in fig.4.7 is not consistent with the few per cent variations between pixels discussed in the PMT manual. It is important for a better calibration of the spectrometer to repeat the study using a more stable and uniform light source.

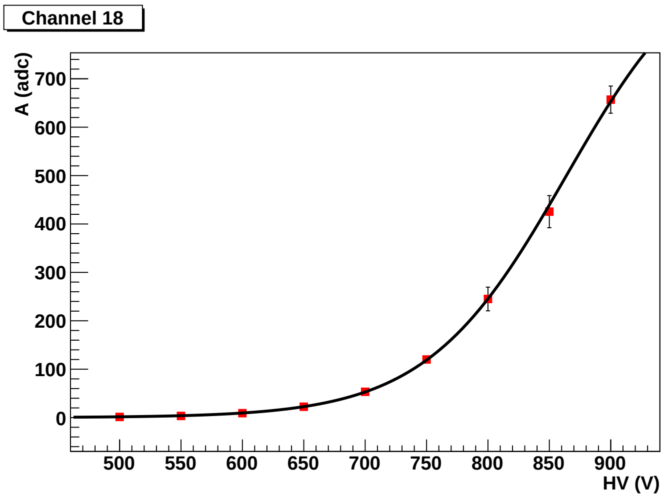

Figure 4.9. Single channel not-normalized ADC counts as a function of the HV tension. Again, data are in red boxes, fit result is in black curve.

4.2 Tests and Calibrations

The Beam Test Facility (BTF, [20]) is part of the DAΦNE Φ-factory complex, the most recent of the electron-positron colliders in the long history of the INFN Laboratori Nazionali di Frascati (LNF). The facility features a high-intensity linac that provides electrons and positrons up to 750 MeV and 550 MeV respectively, a damping ring to improve injection efficiency and two main rings designed for the abundant production of K mesons coming from the decay of the Φ resonance at 1.02 GeV.

Before the high-intensity electron or positron beam pulses produced by the 60 m long linac are injected into the double storage ring, they can be extracted to a transfer line that is dedicated to the calibration of particle detectors, the characterization and calibration of beam diagnostics, and the study of low-energy electromagnetic interactions. Here, the number of particles can be reduced to a single electron or positron per pulse by means of a variable thickness copper target.

The particle momentum is then selected, with an accuracy better than 1%, using a dipole magnet and a set of tungsten collimators. The energy range is typically 25-500 MeV, and up to 49 pulses per second can be extracted (20 ms repetition time), with a bunch length of 10 or 1 ns. When not operating in conjunction with the collider, the linac's maximum beam energy can be raised to 750 MeV (for electrons) and the intensity increased to a maximum of 10^{10} particles per second, limited by radiation safety.

4.2.1 Validation of the magnetic field map and focusing property

A first test done at the BTF is the validation of the magnetic field map discussed in sec.3.1.1. Fig.4.10 shows the experimental setup used. To measure the deflection of the electrons (198 MeV) we use two arrays of scintillating fibers placed in air, one

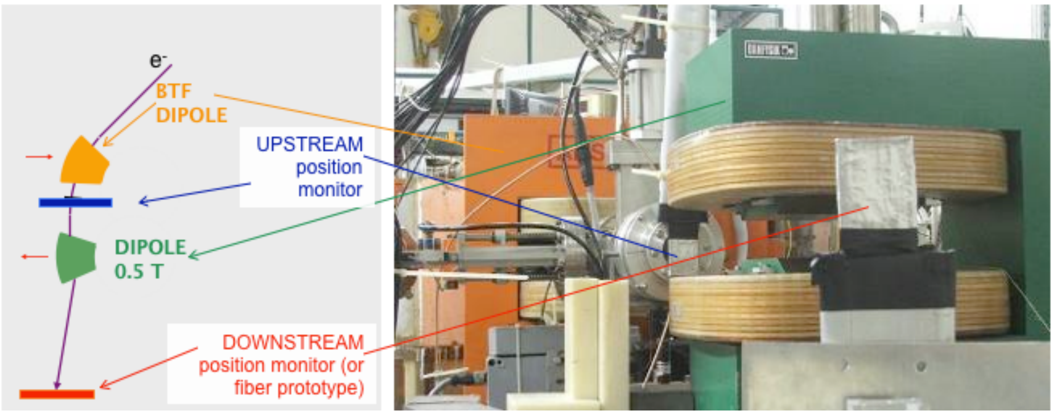

Figure 4.10. Experimental set-up for the validation of the magnetic field map measurements: the green dipole is the one used for the PlasmonX experiment. Wrapped in aluminum foil are the scintillating fibers detectors placed immediately after the beam pipe, for the initial electron position measurements, and after the dipole to detect the deflected position.

before and one after the bending magnet. Electrons propagate in x direction and are deviated along the y axis. In order to scan the whole dipole length, the magnet is placed on a sliding table and moved with respect to the electron beam. Fig.4.11

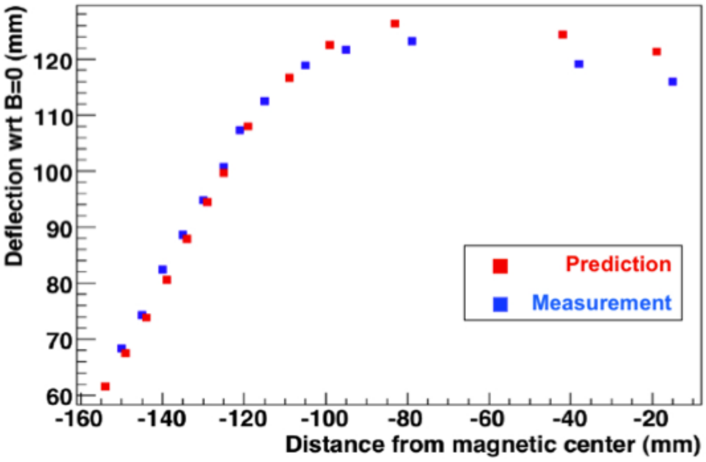

Figure 4.11. BTF test: observed (blue boxes) and predicted (red boxes) electrons beam deflection as a function of the distance from the magnetic center.

shows the measured deflection with respect to the distance from the magnetic center: in blue are experimental data, in red prediction done using Runge-Kutta integration method. The good agreement in the fringe region of interest (from 10 to 15 cm far away from the center) and the importance of an accurate alignment are clear.

A second test done at the BTF consists in the measurement of the electron beam spot size as a function of the distance from the magnetic center. We expect the spot size to shrink in the fringe area (from 10 to 15 cm far away from the magnetic center) because of the focusing property. The experimental set-up is similar to the one discussed above and the measurements are done in air: the main contribution to the angular divergence of the beam is the multiple scattering.

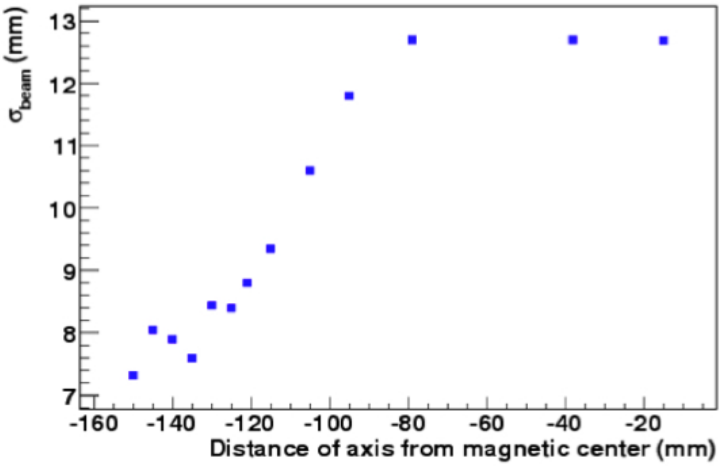

Figure 4.12. BTF test: electron beam spot size measurements as a function of the distance from the magnetic center. The fringe focusing effect is observed.

Fig.4.12 shows the obtained results: keeping increasing the distance from the center of the magnet the beam spot size reduces.

4.2.2 Saturation studies

The charge $Q_{measured}$ measured by the detector is proportional to the number of particles $N_{particles}$ impacting the fibers times the number of photo-electrons $N_{phe/particel}$ generated times the gain G_{PMT} of the PMT times the gain G_{el} of the electronics. In formula we have:

$$Q_{measured} = N_{particles} \times N_{phe/particel} \times G_{PMT} \times G_{el} \tag{4.4}$$

where the last three terms can be tuned, increasing or decreasing the signal. This allows to avoid saturation effects and in this section we will discuss that point.

The electronic saturation occurs when ~2400 ADC counts are integrated, which means, subtracting the pedestal values, ~600 ADC counts. Fig.4.13 shows a scan in electronic gain parameter. Scanning values from 2 to 64, the response is expected to span a range of 32: here we observe that the Maroc2 saturation does not allow to have more that ~ 2400 counts. We conclude that the dynamic range of the acquisition devise is about 600 units.

The phototube saturation has been studied measuring the PMT response to increasing electron beam charge. The study is done at the BTF, Frascati. Setting the PMT high voltage value at 600 V, we acquire the beam profile observed on the fibers. The electron beam charge is measured by a toroid. We did two measurements:

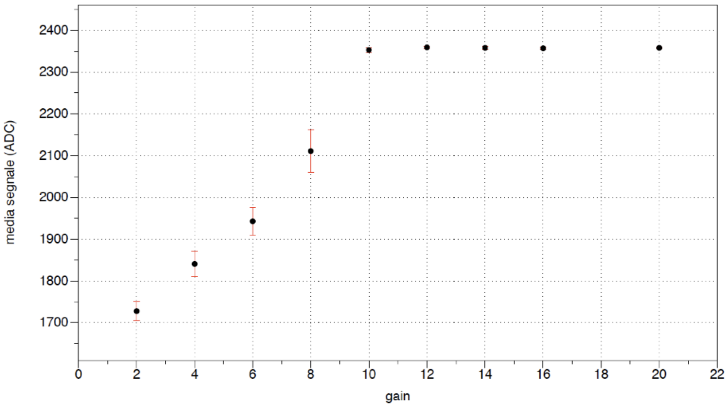

Figure 4.13. ADC counts versus electronic gain.

with 120 and 240 pC electron charge. The detector response is very similar while it is expected the total ADC counts to double. We can also exclude the saturation of the electronic read out because of the fact that the maximum ADC count observed is below the saturation value (∼800 counts).

To work with high electron charge requires to lower the PMT tension which means the gain of the PMT: we have observed exactly the same whole spatial distribution but reduced by a global factor when the tension is decreased by 100 V.

If during the PlasmonX experiment to work with the lowest electronic gain and PMT tension is not enough to avoid saturation effects, we can reduce the number of photo-electrons by a know attenuation factor. This can be done using a calibrated neutral density filter to insert between the bundle of fibers and the PMT, at the entrance of the photo-tube.

4.2.3 Calibration in charge

The last aspect we want to discuss is the measure of the linearity of the detector response at high electron beam charge. This study is done at the BTF, Frascati.

During these tests we used electron beams of 500 MeV and charges from the pC to the nC range. The beam charge is measured by an Integrating Current Transformer (ICT) toroid (Bergoz, 10:1 transformer ratio, 30 ns risetime, see fig.4.14), and the beam spot independently measured by means of a high fluorescence flag readout by a videocamera.

The scintillating fibers of the prototype are placed perpendicularly to the electron beam, at a distance of ∼20 cm, and readout by our standard MAROC electronics. Whole the electronics is placed inside a Faraday cage so to be shielded from the electromagnetic noise produced on the electrons beam path (see fig.4.15). The profile of the beam was clearly visible and compatible with the measured beam-spot.

Using a neutral density filter with attenuation factor 0.4%, applying 400 V to the PMT and setting the gain of the electrons to an intermediate value (MAROC g=8, 0.5×) we observe the detector response shown in fig.4.16. From top to bottom the toroid measured charge is 0.16, 0.22, 0.46 nC. To obtain the total fiber charge

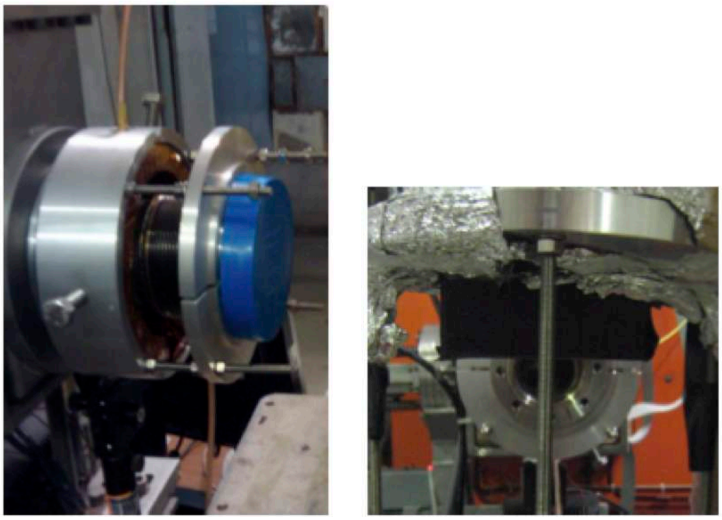

Figure 4.14. BTF test: lateral view of the toroid used for the beam charge measurement on left; view of the prototype placed in front of the toroid at a distance of ∼20 cm. The device is in air.

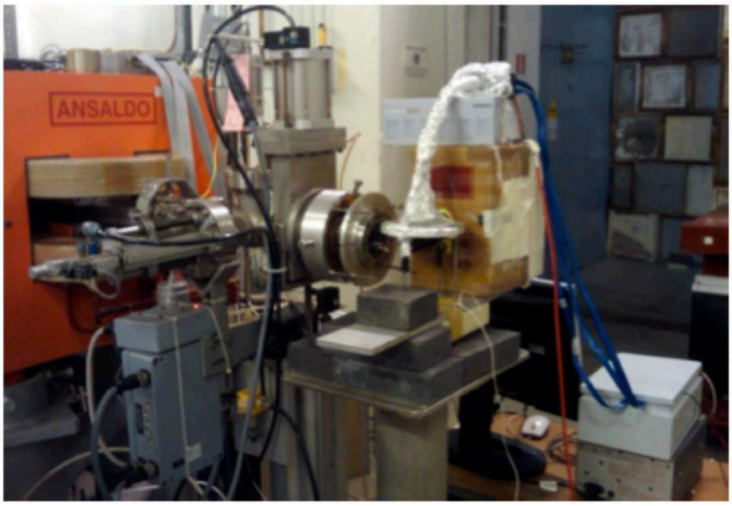

Figure 4.15. BTF test: prototype, wrapped in aluminum foil, placed after the ICT for charge calibration measurements.

we have to integrate counts over the 64 fibers: a linear response of the detector with respect to the beam charge is observed up to ∼0.2 nC, as shown in fig.4.17. A fit function given by

$$f(x) = p_0(1 - e^{-x/p_1}) \tag{4.5}$$

is used to study the calibration result. For low beam charge this behaves linearly with slope given by $p_0/p_1 \sim 120$. When the electron beam charge increases the expected linearity is lost probably due to saturation effects, again.

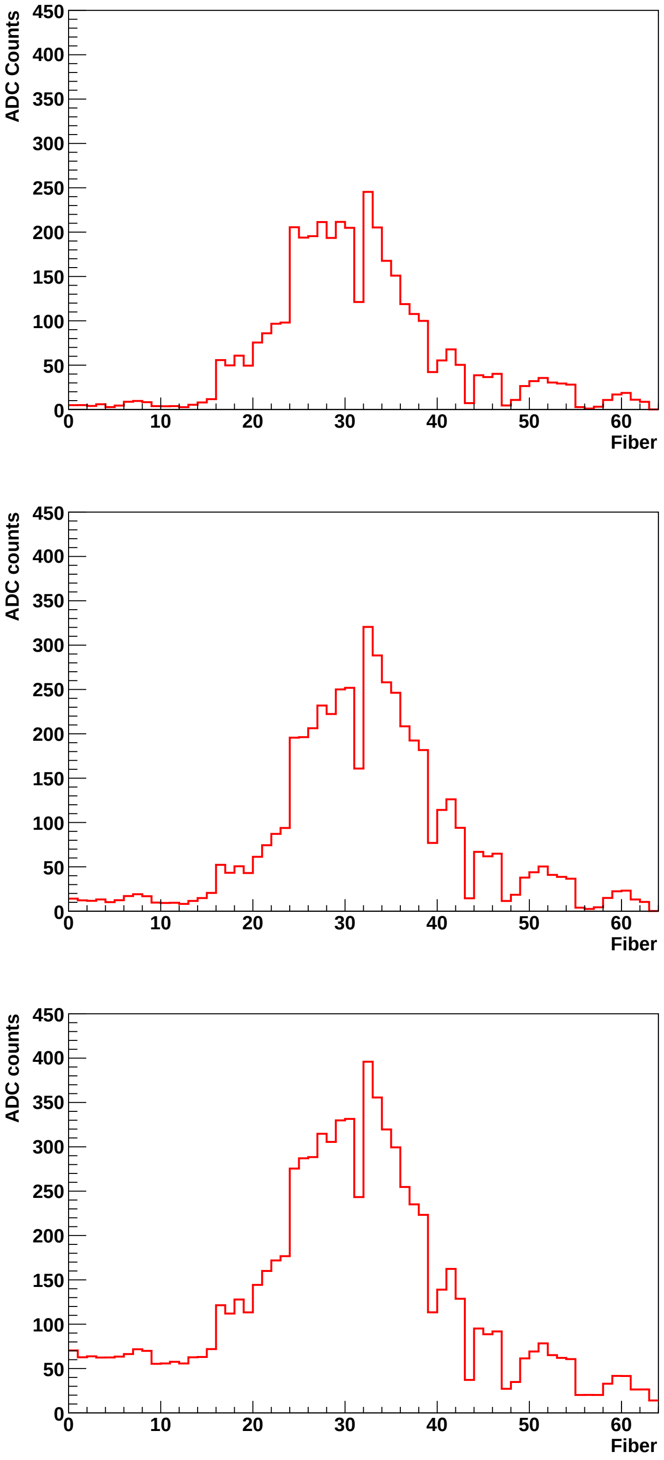

Figure 4.16. Electron charge scan: increasing the beam intensity, fiber charge increases. Here we use a 0.4% neutral density filter, PMT HV=400 V, intermediate electronics gain. From top to bottom we have 1, 1.5, 3 $\times 10^9$ electrons per beam as measured by the toroid.

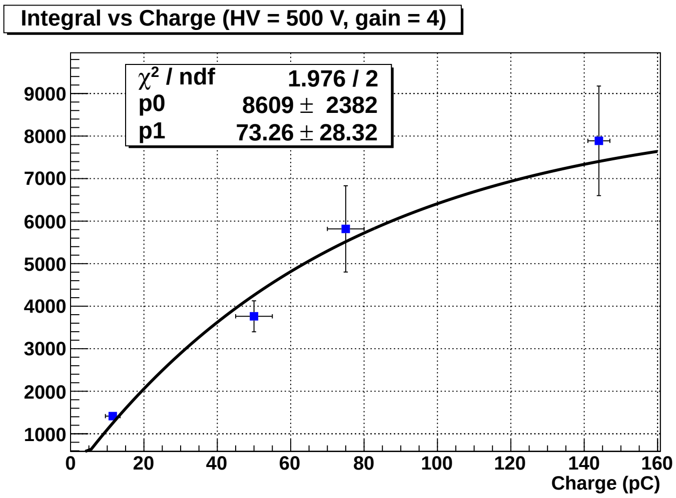

Figure 4.17. Calibration of the fiber detector signal as a function of the beam charge measured by the ICT, with 500 MeV electrons from the BTF line.

Chapter 5

First experimental results

In the previous chapters we have discussed experimental tests for calibration purposes. Here we present the first results obtained by the SITE experiment. The aim of the measurements done is to demonstrate that the whole experimental setup is working and accelerated electrons can be produced. Problems with the too high electromagnetic noise arose and for this reason we could not operate with the purely electronic acquisition system. In this temporary setup we were forced to use a purely optical device. The electronic read-out, together with the improvements made and discussed in this chapter, will be tested as soon as the commissioning resumes and specifics noise studies will be performed.

The final claim of the measurements done is the observation of electron acceleration in laser plasma interaction using the FLAME laser at the LNF laboratories.

In this chapter the problems we come across with and the solutions taken in order to quantify the energy distribution of the very preliminary accelerated bunches are discussed.

5.1 Commissioning set-up: inside the interaction chamber

In Fall 2010 the commissioning started and the first electron bunches were accelerated, with low laser intensity and preliminary experimental conditions.

Fig.5.1 shows the general experimental set-up. The laser is coming from right to left and electrons are accelerated in the forward direction. A round – 5 cm diameter – Lanex screen is placed at a distance of 35 cm far from the gas jet nozzle, rotated at 45° with respect the laser beam direction, so to allow the placement of a CCD camera without disturbing the path of the accelerating electrons. The Lanex is shielded by a 50 μm aluminum foil. We use three CCD cameras for diagnostic and alignment purposes. Two CCDs are used for the scattering Thomson (see sec.2.1): we collect simultaneously lateral and top images of the gas-jet. As it can be seen from the side view of the interaction chamber (see fig.5.1), the third one is pointing to the Lanex so to allow a measurement of the laser pointing stability and of the divergence of the accelerated electrons bunch. Fig.5.2 is a picture of the experimetal set-up inside the interaction chamber.

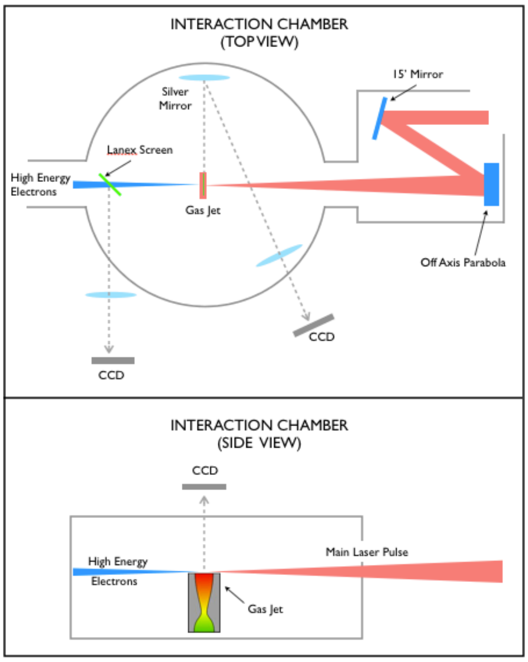

Figure 5.1. Schematic view of the set-up during the first laser-plasma interaction test experiments.

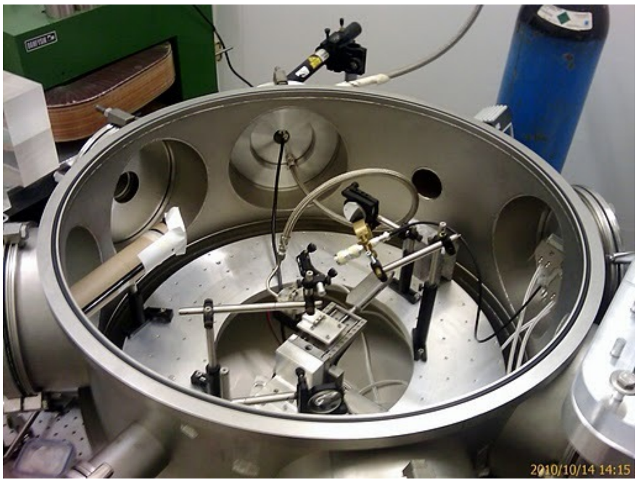

Figure 5.2. Experimental set-up Inside the interaction chamber.

The laser energy is about 1 J in 30 fs, corresponding to a power of $\sim$ 30 TW. It is sent on a N_2 gas jet (gas pressure 10 bar). At the entrance of the nozzle the measured intensity is $6.2 \times 10^{18} W/cm^2$ with $r_0 \sim 13\mu m$. These parameters define a non linear regime being $a_0 \sim 1.7$, as defined in sec.1.1.4.

5.2 Electromagnetic noise

The first attempt to measure the electrons energy distribution is done using the spectrometer with the electronic read out system. The electronics is placed on the back side of the dipole (see fig.5.3), at a distance of ∼1.5 m far away from the interaction point inside the vacuum chamber. The electronics readout proved to be not screened enough from the pulsed high energy field generated in the laser-plasma interaction, making it impossible to discriminate signal from noise. The readout dynamic range limits signal on PMT to ∼1 V; in design conditions of screening we have noise of ∼1 V peak-to-peak.

The whole set-up, perfectly operating with high energy and high intensity electron beams, suffers the electromagnetic noise arising from the laser-plasma interaction.

We have evaluated the electromagnetic noise under different experimental conditions and studied its behavior in detail.

The large noise is induced on the PMT and electronics chain exclusively when both the laser and the plasma are present: this indicates that the noise is plasma related. In absence of either gas or laser the noise is negligible − of the order of few mV.

What we can conclude studying the nature of the noise is here listed:

- the high voltage applied to the PMT is irrelevant, we have the same response working at 0 V and 500 V;
- we observe a reduction by 30% when the PMT is oriented towards the interaction point−when normally is orthogonal to the laser direction;
- with simple improvements in screening (wrapping with aluminum foil) and getting further away (∼2 m) from the interaction point we obtained a reduction of a factor 4.
- a lead shield reduces the response by a factor 6;
- we observe improvement by a factor ∼15 when the PMT is placed behind a radio protection wall. In this way both the distance and the screening are impoved.

It is worth to stress once again that this was the first attempt of using a not purely optical device in a laser-plasma interaction environment. To reduce the electromagnetic noise the following initiatives have been taken:

- extend fiber length in order to place PMTs and electronics far away from the interacting region, behind the radio-protection wall;
- attenuate the signal at the entrance of the Maroc2 chips with specially realized attenuators, in order to increase the signal to noise ratio;
- improve the grounding of the whole system;
- realize better Faraday cases for the PMTs and electronics.

This improvements will be tested as soon as the commissioning resumes and further noise studies will be performed.

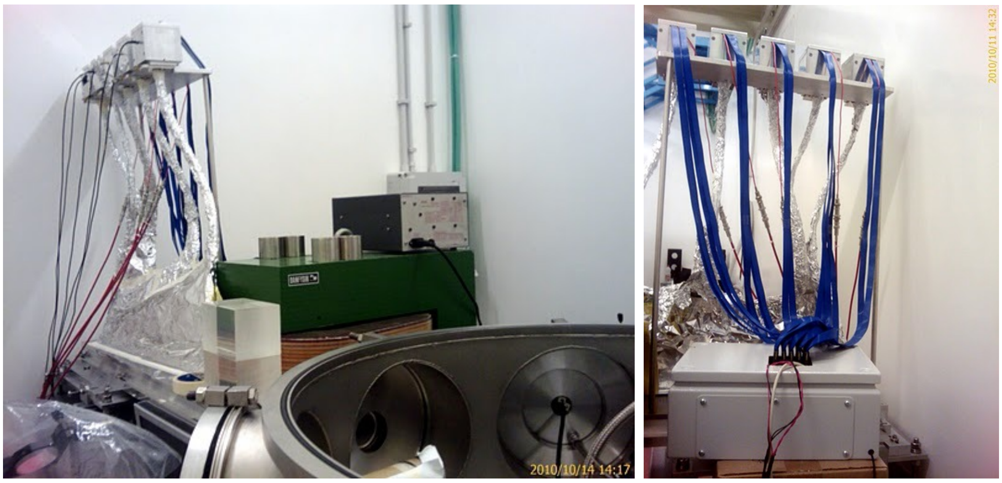

Figure 5.3. Electron spectrometer during the commissioning tests.

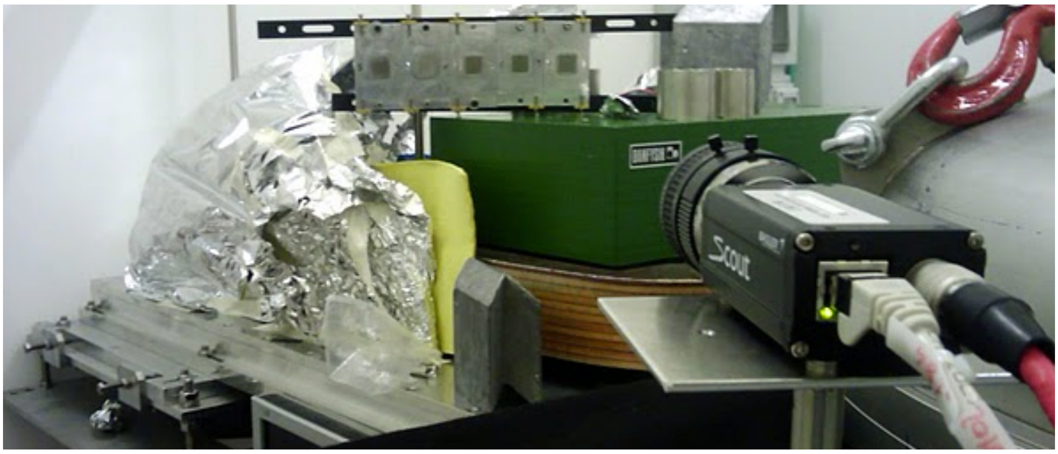

Figure 5.4. Experimental set-up during the first laser-plasma interaction test experiments.

5.3 CCD read-out system

Fig.5.4 shows the alternative read-out set-up realized during the commissioning. We used three CCD cameras, each one reading one fiber bundle by taking a picture of the fiber mask where the PMT has been removed. The bundles analyzed were the two corresponding to the high momentum detector and the one corresponding to the low momentum detector farthest from the interaction point (see fig.3.17). We chose to measure the signal only in this part of the detector because we expected low energy electrons. The magnetic field during the acquisition was set to 50 mT.

5.4 Observed spectra

The image-reconstruction based analysis tools characterize the CCD response taking into account aspects as the different gains of the scintillating fibers and the possible

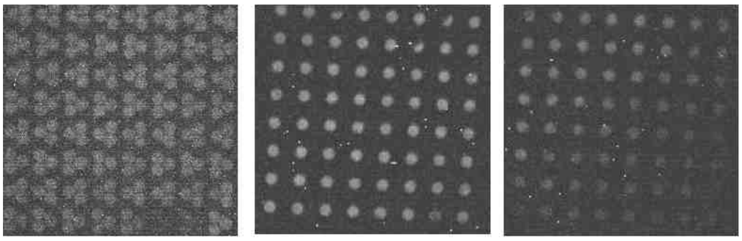

Figure 5.5. Portion of the simultaneously taken CCD images where the signal is clearly visible. The three images represents the fibers response to a single laser shot.

inclination between the CCD lens and the fibers area. Once the experimental parameters are fixed, we need to define the position of the fibers on the CCD images. This is done once – before the data taking – using a LED to illuminate the fibers. The software recognizes the position of the fibers corresponding to a single PMT channel using the different intensity between the illuminated pixels and the dark areas. The obtained 64-boxes matrix is then applied over each data image and each box is mapped into the corresponding fiber position.

Fig.5.5 shows a portion of the CCD row signal images where the electron signal is visible. The images are simultaneously taken and correspond to a single event of laser plasma interaction. The light spots correspond to the scintillating fibers and the intensity is proportional to the impacting electron charge. Starting from right to left it is clearly observable the electron deflection (the fibers follow a zig-zag pattern).

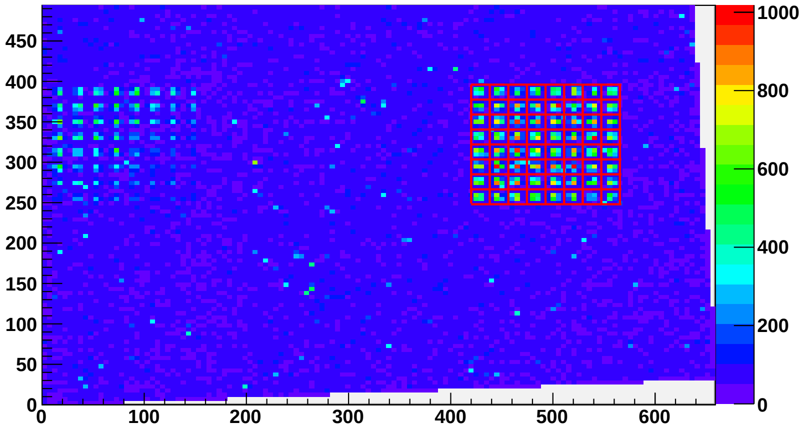

Figure 5.6. Data analysis: mask applied on the CCD image. Making use of existing cameras and read-out software we have developed the code to extract the light per fiber and translate it into an energy spectrum.

Fig.5.6 shows the 8×8 mask applied on each region where the signal is present. The CCD pixel response is a number in the range $(0-255)$. For a given box of the matrix, the pixels intensities are summed: the distance between the CCD camera and the fibers (∼40 cm) is enough to avoid saturation effects.

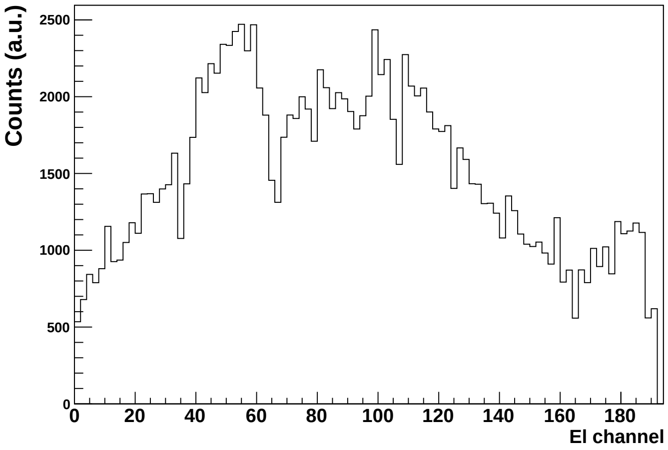

Figure 5.7. Position spectrum: CCD counts versus position in the detector. This is the resul of the pixel-fiber mapping once the inter-calibration of the CCDs is applied.

This procedure, repeated for the three CCD in use, gives us the position spectrum, CCD counts versus position on the detector, shown in fig.5.7.

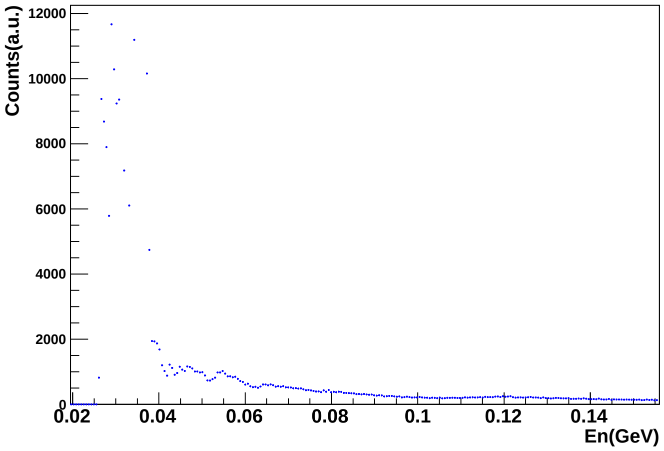

Figure 5.8. Energy spectrum: example of broad energy distribution obtained unfolding plot in fig.5.7

The procedure used to unfold the energy distribution is the Bayesian approach discussed in sec.3.2.2. Fig.5.8 shows the unfolded energy spectrum for the observed images shown in fig.5.5. The shape is characterized by broad distribution at low energies and a long tail above 100 MeV. This is expected since the laser-plasma setup was not optimized.

Chapter 6

Summary

This thesis is in the framework of the new acceleration techniques, i.e. the search for alternatives to conventional particle accelerator technology. I've collaborated in the PlasmonX project developed at the Laboratori Nazionali di Frascati. In particular the research of the group I've worked with is about a device able to measure the electrons produced in the laser-plasma experiment that is part of the PlasmonX project. The main challenging aspects are the three orders of magnitude in energy spread, the large angular divergence and the high number of electrons of the produced bunch.

The electron spectrometer designed is composed of a dipole that deflects the electrons and an array of scintillating fibers used for the position measurement. The signal produced by the charged particles impacting the scintillating fibers is collected by photomultipliers and translated in ADC counts by an electronic read out system.

Using electron beams with characteristics close to those expected in the PlasmonX experiment the spectrometer has been characterized during experimental tests done both in the university laboratory and at the Beam Test Facility at Frascati.

The response of the spectrometer has been studied using both a fast simulation based on Mathematica tracking codes and on Geant4 full simulation. The result I found is that we have a good energy resolution ($<5\%$) up to $\sim$300 MeV.

In the fall 2010 the first laser-plasma acceleration experiment has been done. The whole set-up, perfectly operating with high energy and high intensity electron beams, suffers the electromagnetic noise arising from the laser-plasma interaction. Using a purely optical read out system we were able to observe the first accelerated electrons at the facility of Frascati.

Bibliography

[1] T. Tajima and J. M. Dawson, "Laser electron accelerator," *Phys. Rev. Lett.*, vol. 43, pp. 267–270, Jul 1979.

[2] E. Esarey, C. B. Schroeder, and W. P. Leemans, "Physics of laser-driven plasma-based electron accelerators," *Rev. Mod. Phys.*, vol. 81, pp. 1229–1285, Aug 2009.

[3] T. Tajima and J. M. Dawson, "Laser electron accelerator," *Phys. Rev. Lett.*, vol. 43, pp. 267–270, 1979.

[4] F. Chen, *Introduction to Plasma Physic and Controlled Fusion Plasma Physic.* Springer, 1984.

[5] W. Kruer, *The physics of laser plasma interaction.* Addison-Wesley Publishing Company, 1988.

[6] T. Katsouleas *Nature*, vol. 431, p. 515, 2004.

[7] J. van Tilborg, C. B. Schroeder, C. V. Filip, C. Tóth, C. G. R. Geddes, G. Fubiani, R. Huber, R. A. Kaindl, E. Esarey, and W. P. Leemans, "Temporal characterization of femtosecond laser-plasma-accelerated electron bunches using terahertz radiation," *Phys. Rev. Lett.*, vol. 96, p. 014801, Jan 2006.

[8] W. Leemans *et al. Phys. Plasmas*, vol. 11, p. 2899, 2004.

[9] S. Mangles *et al.*, "Monoenergetic beams of relativistic electrons from intense laser-plasma interactions," *Nature*, vol. 431, p. 535, 2004.

[10] C. Geddes *et al.*, "High-quality electron beams from a laser wakefield accelerator using plasma-channel guiding," *Nature*, vol. 431, p. 538, 2004.

[11] W. Leemans *et al. Nat. Phys.*, vol. 2, p. 696, 2006.

[12] k. Nakamura *et al. Phys. Plasmas*, vol. 14, 2007.

[13] D. Giulietti *et al.*, "PlasmonX Conceptual Report,"

[14] D. Alesini *et al.*, "The SPARC project: a High brightness electron beam source at LNF to drive a SASE-FEL experiment," *Nucl. Instrum. Meth.*, vol. A507, pp. 345–349, 2003.

[15] L. A. Gizzi *et al.*, "Laser-plasma acceleration with self-injection: a test experiment for the sub-PW FLAME laser system at LNF- Frascati," *Nuovo Cim.*, vol. C32N3-4, pp. 433–436, 2009.

[16] D. Strickland and G. Mourou, “Compression of amplified chirped optical pulses,” *Opt. Comm.*, vol. 56, pp. 219–221, 1985.

[17] C. Benedetti, “Simulation of particle acceleration in PlasmonX project,” *AIP Conference Proceedings*, pp. 11–14, 2009.

[18] P. Barrillon, “MAROC: Multi Anode Readout Chip,” p. 26, 2007.

[19] G. D’Agostini, “A Multidimensional unfolding method based on Bayes’ theorem,” *Nucl.Instrum.Meth.*, vol. A362, pp. 487–498, 1995.

[20] G. Mazzitelli *et al. Nicl. Instrum. Meth*, vol. A 515, p. 524, 2003.